

Entanglement Diagnostics for Efficient Quantum Computation

Joonho Kim¹ and Yaron Oz^{1,2}

¹School of Natural Sciences, Institute for Advanced Study, Princeton NJ, USA

²Raymond and Beverly Sackler School of Physics and Astronomy, Tel-Aviv University,
Tel-Aviv 69978, Israel

March 24, 2022

Abstract

We consider information spreading measures in randomly initialized variational quantum circuits and construct entanglement diagnostics for efficient quantum/classical hybrid computations. Following the Renyi entropies of the random circuit's reduced density matrix, we divide the number of circuit layers into two separate regions with a transitioning zone between them. We identify the high-performance region for solving optimization problems encoded in the cost function of k -local Hamiltonians. We consider three example Hamiltonians, *i.e.* the nearest-neighbor transverse-field Ising model, the long-range transverse-field Ising model and the Sachdev-Ye-Kitaev model. By analyzing the qualitative and quantitative differences in the respective optimization processes, we demonstrate that the entanglement measures are robust diagnostics that are highly correlated with the optimization performance. We study the advantage of entanglement diagnostics for different circuit architectures and the impact of changing the parameter space dimensionality while maintaining its entanglement structure.

1 Introduction

Noisy Intermediate-Scale Quantum (NISQ) technology is being developed rapidly and poses a great challenge to come up with efficient quantum algorithms that will run on the NISQ computers and perform better than classical ones (for a brief review, see [1]). Many real-world use cases are associated with machine learning and optimization, for which random circuits offer an appropriate framework. The typical optimization tasks can be formulated as a search for the ground state of a κ -local Hamiltonian H , which is a sum of local operators that act on κ qubits. The Hamiltonian encodes an exact combinatorial problem. The ground state is an eigenstate of the Hamiltonian with the lowest eigenvalue. The expectation value E of the Hamiltonian defines the cost function. The optimization task is the minimization of the cost function trying to reach the ground-level energy. Stated differently, one can expand any state in the basis of the eigenfunctions of the Hamiltonian, and we are searching for a state with a significant overlap with the ground state (see, e.g. [2]).

The quantum/classical hybrid algorithms consist of two parts. The first part is quantum, where one runs a random quantum circuit made of L layers of quantum gates acting on n qubits. We depict in Figure 1 the circuit architecture that we will use. The initial state will be a simple product state of n qubits, $|0\rangle^{\otimes n}$, acted upon by the quantum gates that depend on a set of nL random parameters, θ , drawn from the uniform distribution. The quantum circuit is a unitary operator $U(\theta)$ that evolves the initial state into:

$$|\psi_c(\theta)\rangle = U(\theta)|0\rangle^{\otimes n} . \quad (1.1)$$

The second part of the hybrid algorithms is classical, where one constructs the cost function of the problem:

$$E(\theta) = \langle \psi_c(\theta) | H | \psi_c(\theta) \rangle , \quad (1.2)$$

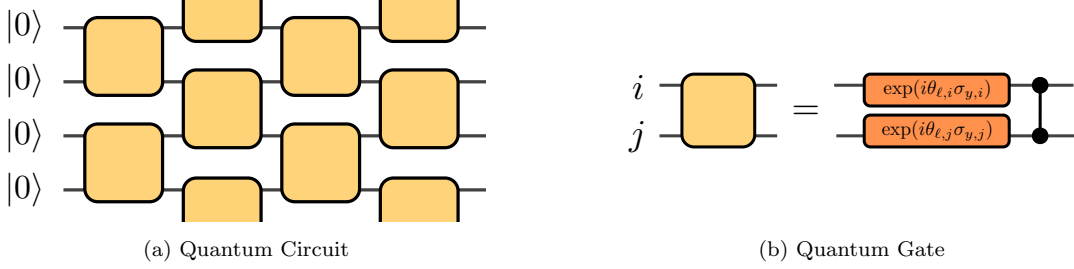


Figure 1: (a) The architecture of the random quantum circuit that we will work with. The vertical axis specifies the n qubits. It can be viewed as a discrete periodic spatial coordinate, i.e. we identify the qubits $i \simeq i + n$. The initial state of the qubits is a product state $|0\rangle^{\otimes n}$ depicted on the left. The horizontal axis denotes the time steps (layers) and the 2-qubit unitary gates' action alternates between the $(i, i - 1)$ and $(i, i + 1)$ pairs of qubits. (b) The structure of the 2-qubit unitary gate. $\sigma_{y,i}$ denotes the Pauli y matrix acting on the i 'th qubit ($1 \leq \ell \leq L$). The parameters $\theta_{\ell,i}$ are drawn randomly from a uniform distribution. The Pauli rotation is followed by an entangling controlled-Z gate.

and minimizes it in the nL -dimensional parameter space using e.g. a gradient descent method. As is clear from the construction, the way for the hybrid algorithms to do better than classical ones is if the quantum circuit can produce effectively a state $|\psi_c(\theta)\rangle$ in the vicinity of the ground state $|\psi_g\rangle$ of the Hamiltonian, using a minimum required number of circuit layers. This paper aims to quantify the vicinity range of L using quantum information measures.

From the physical point of view, the random circuit model is a unitarily evolving closed (1+1)-dimensional chaotic system, where we neglect interaction with a surrounding environment. The discrete space and time directions are spanned by the qubits and the circuit layers, respectively. The initial state $|0\rangle^{\otimes n}$ is pure, and so is the final state $|\psi_c(\theta)\rangle$ produced by the circuit. However, while the initial state is not entangled, the successive application of the circuit layers generates entanglement between the qubits in the final state. Entanglement encodes information in the correlations between the qubits. The higher the entanglement is, the larger the information spread, such that we can read the information only after measuring a significant fraction of the qubits. As we will show, entanglement is responsible both for the success and failure of the quantum algorithms. The quantum algorithm will not be effective in the absence of entanglement, as well as with its excess. We will quantify an optimal region of information spreading and entanglement, which leads to the success of the optimization in the quantum/classical hybrid algorithms.

It will be convenient to work with the density matrix of circuit states, $\rho_c(\theta) = |\psi_c(\theta)\rangle\langle\psi_c(\theta)|$. The circuit's bipartite entanglement can be represented by the reduced density matrix, $\rho_A = \text{Tr}_B \rho_c(\theta)$, obtained by dividing the system of n qubits to two subsets A and B with n_A and $n_B = n - n_A$ qubits, respectively, and taking the partial trace over the degrees of freedom in the subset B . We will mainly work with the equal partition case $n_A = n_B = \frac{n}{2}$. In particular, the k -th Renyi entropy of the reduced density matrix ρ_A ,

$$\mathcal{R}_A^k = \frac{1}{1-k} \log \text{Tr} (\rho_A^k) , \quad (1.3)$$

offers a simple measure of the entanglement between the two subregions, where we use the logarithm with base 2. The limit $k \rightarrow 1$ corresponds to the von Neumann entanglement entropy:

$$S_{EE} = -\text{Tr} \rho_A \log \rho_A . \quad (1.4)$$

We will use these entropies to diagnose the efficiency of the quantum algorithm.

The general structure of the Renyi entropies of the quantum circuit is depicted schematically in Figure 2 as a function of the number of circuit layers. We denote three regions on the plot: A , B and C .¹ In the major part of region A , the entanglement entropies grow linearly in the number of layers L , and this is followed by a change in the functional dependence on the number of layers till saturation. The slope of

¹We use the same symbols A , B also to denote the subsets of qubits. The meaning should be clear from the context.

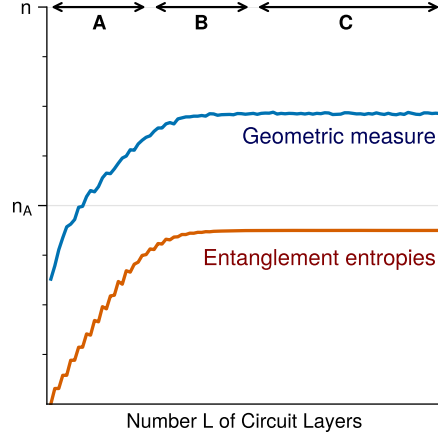


Figure 2: A schematic plot of the entanglement entropies and distance measure growth under the random circuit evolution. The horizontal line denotes the number of circuit layers. We distinguish three regions A, B and C . We will see that a good starting point for an effective optimization with a κ -local Hamiltonian is to use the circuit density matrix from region A . The density matrices in region C are highly entangled and do not provide a good starting point for the optimization. Region B is a transition region and starting with a density matrix from this region leads to an unstable optimization.

the linear curve is the entanglement velocity that depends on the order k of the Renyi entropy (1.3) and the circuit architecture, but is independent of the number of qubits n_A . The entanglement curve in the region B undergoes the transition to the maximal plateau that corresponds to the region C . We will later identify the density matrices of the quantum circuits in the region A as leading to efficient optimization. On the other hand, we will show that the circuit density matrices in regions B and C are not suitable for an efficient algorithm. Physically, the entanglement entropy in the linear growth of region A follows the area law, while those in the regions B and C exhibit the volume law, i.e., a scaling with the system size n_A up to an additive numerical constant. Since a ground state of κ -local Hamiltonians is typically a non-generic state whose entanglement entropy follows the area law, the density matrices in the regions B and C are far away from the ground state. This makes the density matrices of the regions B and C not useful as a starting point for optimization in the quantum/classical hybrid algorithms. As we will see, the transitional nature of the region B appears as the circuit's instability under the gradient descent optimization, where individual outcomes exhibit high variability from success to failure.

It has been argued in [3] that for a large class of random quantum circuits the average value of the derivative of the energy function vanishes, hence creating a problem for using the gradient descent method known as the barren plateau. The probability of deviating from the vanishing average gradient is exponentially small in the number of qubits. The underlying assumption in the analysis of [3–5] is that the random circuit unitary ensemble is a quantum 2-design, meaning that the first and second moments are indistinguishable from the Haar random distribution. In general, the k -th Renyi entropy (1.3) serves as a diagnostic for how close a unitary ensemble is to the quantum k -design [6]. If the averaged entropy cannot be distinguished from that of the Haar random distribution, it implies the unitary ensemble virtually possesses the k -design structure. This is indeed the case for circuit unitaries that belong to the regions B and C in Figure 2, where the Renyi entropy is maximized to the subsystem size n_A up to a small constant shift. From our viewpoint, the vanishing gradient problem is still secondary to the real issue that impedes efficient optimization; circuit states in the regions B and C are simply too far from the vicinity of the ground state, such that developing an optimization path to the ground state demands generically an exponentially large parameter space [7].

The complexity of Haar random states is exponential in the number of qubits. In contrast, the k -design distribution can be generated only with polynomial complexity [8]. Indeed, we observe in Figure 2 that the saturation of the Renyi- k entropy occurs in time L that scales linearly with the system size. We also see

that the vast majority of the circuit states do not behave efficiently under the hybrid algorithms. Only the density matrices that belong to the region A, produced with a reduced number of entangling gates, can lead to efficient optimization.

A complementary way to see that generic quantum states produced by the quantum circuit are highly entangled is to use the geometric measure of entanglement [9]:

$$\mathcal{E}_g(|\psi\rangle) = -\log \sup_{\alpha \in \mathcal{P}} |\langle \alpha | \psi \rangle|^2, \quad (1.5)$$

where \mathcal{P} is the set of qubit product states. This measures the distance of the state $|\psi\rangle$ from the closest product state. Figure 2 shows that in the random quantum circuit, the geometric measure of entanglement grows with the same pattern as that of the entanglement entropy. Note that the geometric measure is directly calculated from the full density matrix, while the entanglement entropies are computed via the reduced density matrix. We will discuss elsewhere [10] the impact of operator spreading, which is another diagnostic of information spreading, in the context of variational circuits and hybrid algorithms. The details of the schematic representation of the entanglement entropies and the geometric measure in Figure 2 vary according to the choice of circuit architecture, the form of the two-qubit gate, and the random parameters. We will discuss these aspects throughout the paper and how they allow the design of effective density matrices.

The success of the hybrid algorithm depends critically on certain characteristics of the Hamiltonians that we aim to study [4]. To demonstrate that, we will compare three different one-dimensional Hamiltonians: transverse-field Ising model with nearest-neighbor interaction, transverse-field Ising model with long-range two-spin interaction, and the Sachdev-Ye-Kitaev (SYK) model [11–13]. The comparison will demonstrate that the classical optimization works well with initial circuit states that belong to the region A in reaching the ground state energy level of the Ising Hamiltonians that exhibit an area law scaling of the entanglement. In contrast, we will see that irrespective of what is the initial state we start with, the optimization algorithm fails to reach the ground state energy level of the SYK model that possess a volume-law entanglement scaling [14] unless one uses an exponentially large parameter space [7].

As an example of a different circuit architecture we will consider a random application of the control-Z entangling gate with probability $p = \frac{1}{2}$ and study the entanglement structure and the optimization performance. We will find we can achieve the same success of the optimization also with more circuit layers. Complimentary to that, we will assess the importance of the high-dimensional parameter space for the optimization performance while maintaining the entanglement structure. We will do that by imposing restrictions on the circuit parameters and we will show that the optimization performance is affected negatively.

The paper is organized as follows. In Section 2 we discuss the entanglement diagnostics and properties of the reduced density matrices for the circuits in regions A, B and C. In Section 3 we perform a detailed numerical analysis of the circuit entanglement properties as a function of the number of layers and empirically quantify the regions A, B and C. In Section 4 we consider three Hamiltonians, the transverse-field nearest-neighbors Ising, the long-range transverse-field Ising and the chaotic SYK. We analyze the properties of their ground states, i.e. the energy and the entanglement. In Section 5 we perform a classical optimization for reaching the ground state energy levels of the three Hamiltonians and discuss the differences. In Section 6 we consider a different circuit architecture and analyse how it affects the circuit entanglement and optimization performance. In Section 7 we show the effect of imposing restrictions on the circuit parameter space, while keeping the same entanglement structure. Section 8 is devoted to a discussion and outlook.

2 Entanglement Diagnostics

Using the density matrix of the quantum circuit $\rho_c(\theta)$, the expectation value of the Hamiltonian (1.2) reads:

$$E(\theta) = \text{Tr}(\rho_c(\theta)H). \quad (2.1)$$

Our optimization problem requires that we get as close as we can to the ground state energy of the Hamiltonian H by minimizing (2.1). In the first part of the algorithm, we operate the quantum circuit to prepare the

density matrix $\rho_c(\theta_{in})$ as a function of randomly chosen parameters θ_{in} . In the second part of the algorithm, the output state $\rho_c(\theta_{in})$ is used to estimate a parameter update for the next step that moves θ towards the gradient descent direction of (2.1). The ground state energy can be reached as close as possible by multiple iterations of evaluating the density matrix $\rho_c(\theta)$ and updating the parameters via the gradient descent, which will stop at a final point $\theta = \theta_f$. We would like to find the final parameter θ_f such that

$$\text{Tr}((\rho_c(\theta_f) - \rho_g)H) \simeq 0 \quad (2.2)$$

where ρ_g denotes the exact ground state of the Hamiltonian H . A simple upper bound of this approximation error (2.2) follows from the Cauchy-Schwarz inequality

$$\text{Tr}((\rho_c(\theta_f) - \rho_g)H) \leq \|\rho_c(\theta_f) - \rho_g\|_1 \cdot \|H\|_1 \quad (2.3)$$

with the trace norm $\|O\|_1 \equiv \sum_i \lambda_i$, where λ_i are singular values of an operator O , i.e., eigenvalues of $\sqrt{O^\dagger O}$. Clearly, the capability of generating an initial state $\rho_c(\theta_{in})$ in the vicinity of the ground state ρ_g is a key factor of efficient classical optimization. However, we generally do not know the ground state, ρ_g , thus being unable to assess the trace distance $\|\rho_c(\theta_{in}) - \rho_g\|_1$ between the initial and ground states directly. We will also see numerically that the trace distance between the two density matrices can be very sensitive to a slight difference between their energies. In this section, we will discuss the use of entanglement entropies as a distance proxy between $\rho_c(\theta_{in})$ and ρ_g . We will show that this is a robust diagnostic for the optimization success.

To examine the bipartite entanglement property of a quantum state ρ , we divide the n qubit system into two subsystems A and B , whose number of qubits are n_A and n_B , respectively, with $n_A + n_B = n$. The quantum state of the subsystem A is given by the reduced density matrix $\rho_A \equiv \text{Tr}_B(\rho)$, obtained after taking the partial trace of ρ over the Hilbert space of the subsystem B . A useful fact to recall here is that the trace distance is monotonically decreasing under the partial trace of subsystems, i.e.,

$$\|\rho_A - \sigma_A\|_1 \leq \|\rho - \sigma\|_1. \quad (2.4)$$

Inequality (2.4) implies that for an optimized circuit state $\rho_c(\theta_f)$ to approximate the ground state ρ_g well, their reduced density matrices $\rho_{c,A}(\theta_f)$ and $\rho_{g,A}$ should also necessarily be close.

The ground state ρ_g of a κ -local Hamiltonian is generically an entangled state. Yet, it is distinctive from a typical quantum state whose reduced density matrix is very close to the equiprobable maximally mixed state [15]. For instance, the entanglement entropy of the ground state ρ_g is expected to follow the area law, in contrast to typical pure states whose entanglement entropy follows the volume law [16]. Our strategy will be to avoid having a maximally entangled state as an initial circuit state $\rho_c(\theta_{in})$ in order to locate it in the proximity of the ground state and develop a more effortless optimization path under the gradient descent.

Let us characterize an upper bound of the trace distance between the reduced density matrix of an initial circuit state, $\rho_A = \rho_{c,A}(\theta_{in})$, and that of a maximally entangled state, $\sigma_A = 2^{-n_A} I_A$, where I_A is an identity matrix on the Hilbert space of the subsystem A . We start from the Pinsker's inequality:

$$\frac{1}{2} \|\rho - \sigma\|_1^2 \leq S(\rho||\sigma) \quad (2.5)$$

on the trace distance between two states ρ and σ and their relative entropy. Substituting $\sigma_A = 2^{-n_A} I_A$,

$$S(\rho_A||\sigma_A) = n_A + \text{Tr}(\rho_A \log \rho_A) = n_A - S_{EE}(\rho_A), \quad (2.6)$$

such that (2.5) becomes

$$\frac{1}{2} \left\| \rho_A - \frac{I_A}{2^{n_A}} \right\|_1^2 \leq n_A - S_{EE}(\rho_A), \quad (2.7)$$

where $S_{EE}(\rho_A)$ is the Von Neumann entanglement entropy (1.4) of the reduced density matrix ρ_A . The inequality (2.7) implies that we should avoid a circuit state whose reduced density matrix ρ_A closely approaches

the maximum value of the entanglement entropy, i.e., $S_{EE}(\rho_A) \simeq n_A$, since a corresponding ρ_A is inevitably close to the fully mixed state and therefore far from $\rho_{g,A}$. Consequently, those high-depth circuit states that belong to the region B and C in Figure 2 are likely to result in an unsuccessful optimization. Note that highly mixed states are close to each other; If we have two states α_A and β_A that satisfy $\|\alpha_A - I_A/2^{n_A}\|_1 \leq \varepsilon$ and $\|\beta_A - I_A/2^{n_A}\|_1 \leq \varepsilon$, the triangle inequality means $\|\alpha_A - \beta_A\|_1 \leq 2\varepsilon$.

Instead, one should look into the region A of Figure 2, i.e., quantum circuits with fewer layers. These circuit states support the entanglement entropy much less than n_A , being non-generic and likely forming an appropriate class for the classical optimization. From the continuity of the q -entropy to the trace distance [17]

$$|\text{Tr}(\rho^q) - \text{Tr}(\sigma^q)| \leq q \|\rho - \sigma\|_1 \quad (2.8)$$

for $q > 1$, we find that

$$\frac{1}{2q} \left(2^{(1-q)\mathcal{R}_A^q(\rho_A)} - 2^{(1-q)n_A} \right) \leq \frac{1}{2} \left\| \rho_A - \frac{I_A}{2^{n_A}} \right\|_1 \quad (2.9)$$

where $\mathcal{R}_A^q(\rho_A)$ is the q -th Renyi entanglement entropy (1.3) of the reduced density matrix ρ_A . Due to the monotonically decreasing property of the entanglement entropies (1.3) and (1.4),

$$\lim_{q \rightarrow \infty} \mathcal{R}_A^q(\rho_A) \leq \dots \leq \mathcal{R}_A^2(\rho_A) \leq S_{EE}(\rho_A) \leq \lim_{q \rightarrow 0} \mathcal{R}_A^q(\rho_A), \quad (2.10)$$

the LHS of (2.9) does not vanish for an initial circuit state $\rho_c(\theta_{in})$ whose $S_{EE}(\rho_A) < n_A$, thereby keeping the trace distance $\frac{1}{2}\|\rho_c - \sigma\|_1$ from a maximally entangled state σ to have a positive lower bound. A more stringent bound on the trace distance can be identified from the following inequality [18]:

$$|S_{EE}(\rho) - S_{EE}(\sigma)| \leq \frac{1}{2}\|\rho - \sigma\|_1 \log(2^n - 1) + H\left(\frac{1}{2}\|\rho - \sigma\|_1\right) \quad (2.11)$$

where $H(t) \equiv -t \log t - (1-t) \log(1-t)$. Scaling up the (sub)system size, i.e., $n_A \gg 1$, we find that

$$1 - \frac{S_{EE}(\rho_A)}{n_A} \lesssim \frac{1}{2} \left\| \rho_A - \frac{I_A}{2^{n_A}} \right\|_1, \quad (2.12)$$

which serves an asymptotic lower bound of the trace distance $\frac{1}{2}\|\rho_c - \sigma\|_1$. Thus, when optimizing the cost function (2.1) of a κ -local Hamiltonian whose ground state is non-generic and follows the area law entanglement, the entanglement diagnostics (2.7), (2.9), and (2.12) suggest the use of initial circuit states that belong to region A of Figure 2. We will employ these quantum information diagnostics in order to monitor that an initial circuit state $\rho_c(\theta_{in})$ is in the entanglement proximity of the ground state and not too close to Haar random states. A clear advantage of following the entanglement/proximity guideline will be presented later in Section 5.

3 Random Quantum Circuit

In this section, we study the growth of entanglement entropy for the circuit states generated by a random circuit evolution of an initial product state $|0\rangle^{\otimes n}$. Figure 1 is an illustration of the quantum circuit architecture that we use in this paper. It defines a $(1+1)$ -dimensional discrete quantum system, where the n qubits along the vertical axis represent the space, and the L layers along the horizontal axis span the time. The qubits are arranged identically with period n , i.e., $i \simeq i + n$, imposing a periodic boundary condition along the spatial direction. At each time, the system's wavefunction evolves by a chain of the two-qubit unitary gates, acting alternately on all neighboring odd-even/even-odd qubit pairs. The two-qubit gate is made of independent Pauli- y rotations acting on single qubits,

$$R(\varphi) = \exp(i\sigma_y \varphi) = \begin{pmatrix} \cos \varphi & \sin \varphi \\ -\sin \varphi & \cos \varphi \end{pmatrix}, \quad (3.1)$$

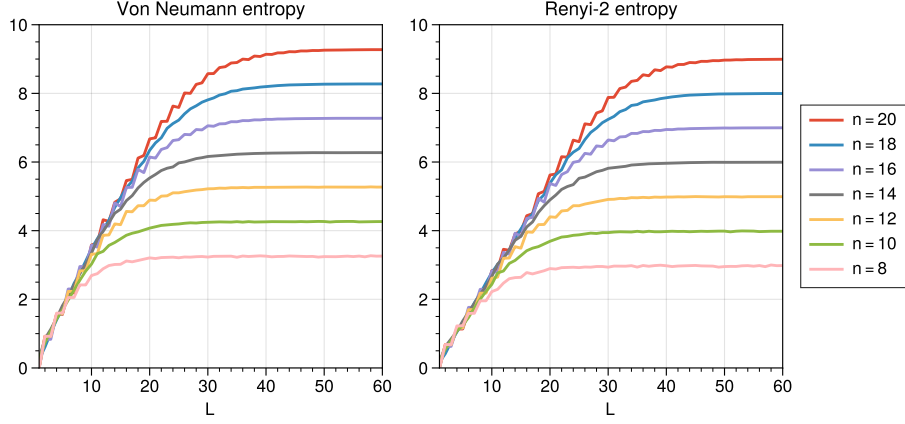


Figure 3: The Von Neumann and Renyi-2 entropies for different numbers of qubits averaged over 50 samples, as a function of the number of layers. We see the linear growth of the entropies to a plateau with an approximate value $\frac{n}{2}$ (up to a numerical shift). The entanglement velocities are independent of the number of qubits but are different for the Von Neumann and Renyi-2 entropies. The Von Neumann entropy plateau is a little higher and the velocity is larger than that of Renyi-2, as expected.

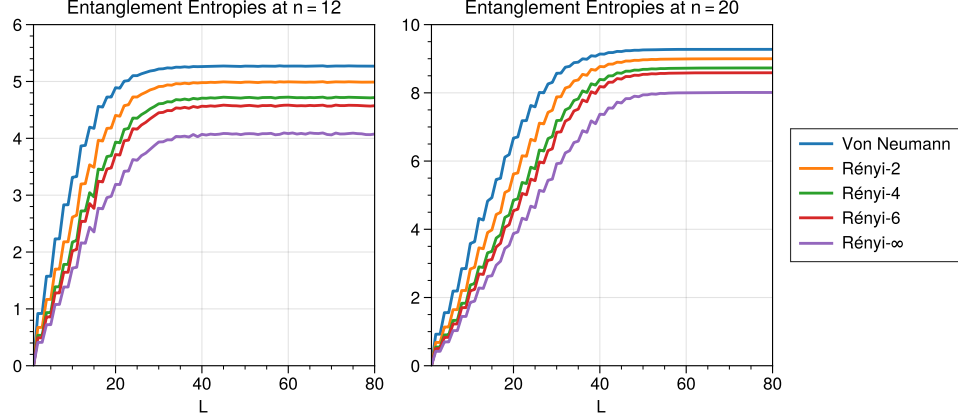


Figure 4: Various k -th Renyi entropies for $n = 12$ and $n = 20$ qubits averaged over 50 samples as a function of the number of layers. We see the linear growth of the entropies to a plateau with an approximate value $\frac{n}{2}$, up to numerical shifts that depend on k . In the linear region, the growth rates are independent of the number of qubits but depend on k .

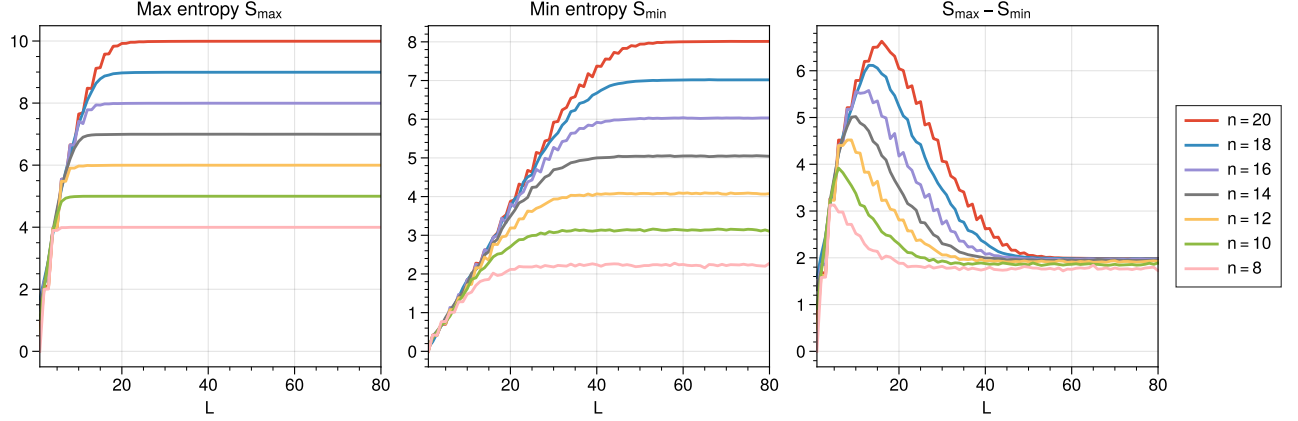


Figure 5: The maximal entanglement entropy growth is the increase of the logarithm of the rank of the reduced density matrix as a function of the number of layers. There is a linear growth with a constant velocity that is independent of number of qubits until saturation at the maximal logarithm of the rank $\frac{n}{2}$. The minimal entanglement entropy growth is the decrease of the largest eigenvalue of the reduced density matrix. We see a slower linear growth until saturation at $\frac{n}{2}$ up to a numerical shift.

followed by the controlled-Z operation

$$CZ = \text{diag}(1, 1, 1, -1) \quad (3.2)$$

that generically creates a pairwise entanglement. We will collectively denote all rotation angles by θ while using $\theta_{l,i}$ to indicate a specific angle that rotates the i 'th qubit at the l 'th layer, for $1 \leq i \leq n$ and $1 \leq l \leq L$. These variables are randomly chosen from an unbiased prior distribution, $\mathcal{U}(0, 2\pi)$, the uniform distribution between 0 to 2π .

3.1 Circuit Entanglement Properties

Consider the evolution of the n -qubit state under the random circuit unitaries of Figure 1 as a function of the discrete-time (number of layers) L . We study the average growth of the random circuit states' bipartite entanglement by decomposing the n qubits into two equal-size subsystems, $n_A = n_B = n/2$, and calculating the sample statistics of several Renyi entropies at different n and L .

Figure 3 shows the Von Neumann and Renyi-2 entropies averaged over 50 random circuit states as functions of the discrete-time L for different number of qubits n . We see the linear growth of the Renyi entropies at early times, whose rate is independent of n . The growth rates slow down and eventually reach the plateaus whose values are the subsystem size $n_A = n/2$ up to negative numerical shifts.

In Figure 4, we compare the Renyi entropies of different order- k 's averaged over 50 random samples. The slope of the linear growth and the negative shift from $n_A = n/2$ of the late-time saturation value depends on the order k but is independent of n . In addition, a higher k leads to a longer saturation time of the Renyi entropy $\mathcal{R}_A^k(\rho_A)$.

It is informative to consider the two limiting cases of the Renyi entropies, i.e., the min- and max-entropies, defined as:

$$\begin{aligned} S_{\max}(\rho_A) &= \lim_{k \rightarrow 0} \mathcal{R}_A^k(\rho_A) = \log(\text{rank } \rho_A) , \\ S_{\min}(\rho_A) &= \lim_{k \rightarrow \infty} \mathcal{R}_A^k(\rho_A) = -\log(\lambda_{\max}(\rho_A)) , \end{aligned} \quad (3.3)$$

where $\lambda_{\max}(\rho)$ is the largest eigenvalue of ρ . In Figure 5 we plot the min/max-entropies averaged over 50 random states. The max-entropy curve expresses the logarithm of the rank of the reduced density matrix ρ_A as a function of L . Its initial growth can be explained by the circuit architecture in Figure 1 that entangles

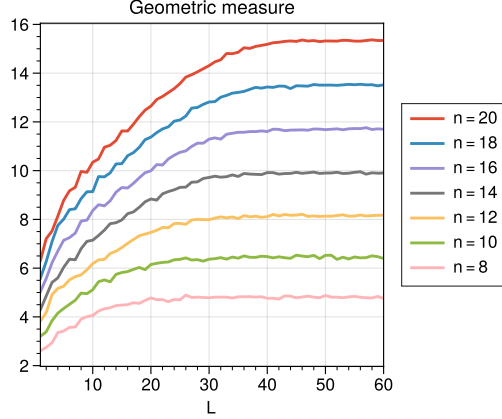


Figure 6: The Geometric measure of entanglement (1.5) quantifies the distance from a product state. We see that the geometric measure for entanglement of the quantum circuit for different numbers of qubits as a function of the number of layers has the same pattern as that of the entanglement entropy.

A with B every second layer. The max-entropy saturates at the maximum possible value, $n_A = n/2$. On the other hand, the min-entropy curve reflects the decrease of the largest eigenvalue of the reduced density matrix as a function of L . Combined with the positiveness and normalization of the density matrix ρ , i.e., $\lambda_i(\rho) \geq 0$ and $\sum_i \lambda_i(\rho) = 1$, it implies that the eigenvalue distribution evolves from having one non-zero λ equal to unity to all λ 's being non-zero and similarly valued, as the discrete-time L increases. Such a spectral change will cause the 2-point spectral form factor for the reduced density matrix ρ_A to develop an early-time decay, a linear ramp, and then a late-time plateau, which are characteristics of the random matrix spectrum [10, 19]. Following the entanglement diagnostics in Section 2, it suggests that we should avoid the circuit states that have already reached the plateau of the min-entropy curve, which typically happens at the timescale $L \sim \mathcal{O}(n)$. Note that the min-entropy curve does not reach the theoretical maximum value $n/2$, and the random circuit states at a very late times are still not maximally entangled.

In Figure 6, we show the geometric measure of entanglement (1.5) that measures the minimum distance from n -qubit product states, averaged over 50 random sample states, as a function of L . The curve exhibits the same growth pattern as that of the entanglement entropies.

3.2 Entanglement Scaling

The presence of the linear growth region in the entanglement entropy curve is a characteristic feature of the global quench dynamics [20], which in our case is caused by the successive application of the layer unitaries $U(\theta_L)$ to the n -qubit product state $|0\rangle^{\otimes n}$. Since the slope of the linear growth is independent of n but varies with the order k of the Renyi entropy, we expect the following area law for the early-time entanglement²

$$\mathcal{R}_A^k(\rho_A) \simeq v_k L \cdot \text{Area}(\partial A) = v_k L, \quad (3.4)$$

where v_k is the entanglement velocity that depends on k . Let us find the linear regression coefficient using the early-time entropies in the range of $0 \leq L \leq n/2$. The estimated values of v_k , computed with different n and k , are summarized in the third column of Table 1. They support two observations that we have seen in Figures 3–5; First, although v_k fluctuates with n , it does not exhibit a dependence on n , thus verifying that the area law (3.4) holds in our random circuit system. Second, $v_{k_1} > v_{k_2}$ for $k_1 < k_2$. We can estimate the number of layer L_l where the linear growth region ends. We define it as the last layer L where the deviation $|\mathcal{R}_A^k(L) - v_k L|$ between the Renyi entropy and its linear approximation is smaller than two times

²The boundary of the line interval has two points, $\text{Area}(\partial A) = 2$. We ignore in (3.4) this factor of 2.

Type	n	v_k	L_l	$r_{n,k}$	L_s	Type	n	v_k	L_l	$r_{n,k}$	L_s
S_{max}	8	0.8534	6	3.9985	9	\mathcal{R}_A^4	8	0.2232	9	2.7084	29
	10	0.9342	6	4.9983	12		10	0.2077	12	3.7101	33
	12	0.8694	8	5.9974	18		12	0.2134	19	4.7177	43
	14	0.8922	8	6.9965	23		14	0.2225	19	5.7234	49
	16	0.8510	9	7.9956	32		16	0.2199	29	6.7272	60
	18	0.8305	10	8.9947	35		18	0.2212	32	7.7290	63
	20	0.8011	11	9.9931	47		20	0.2156	41	8.7299	71
S_{EE}	8	0.3669	7	3.2526	29	\mathcal{R}_A^6	8	0.2050	9	2.5798	27
	10	0.3480	6	4.2639	33		10	0.1911	14	3.5708	33
	12	0.3533	13	5.2703	43		12	0.1963	21	4.5764	41
	14	0.3551	9	6.2743	49		14	0.2057	22	5.5823	49
	16	0.3522	17	7.2766	58		16	0.2031	31	6.5866	60
	18	0.3459	12	8.2776	65		18	0.2046	35	7.5887	63
	20	0.3411	23	9.2781	71		20	0.1995	43	8.5899	71
\mathcal{R}_A^2	8	0.2771	9	2.9722	29	S_{min}	8	0.1724	9	2.2341	23
	10	0.2581	12	3.9821	36		10	0.1611	14	3.1373	33
	12	0.2645	17	4.9896	43		12	0.1651	21	4.0823	39
	14	0.2711	15	5.9944	49		14	0.1739	23	5.0491	46
	16	0.2689	23	6.9973	60		16	0.1715	35	6.0303	53
	18	0.2682	24	7.9986	65		18	0.1726	39	7.0181	60
	20	0.2619	33	8.9993	71		20	0.1686	49	8.0118	66

Table 1: Phenomenological analysis of the entanglement structure of the random quantum circuit. The entanglement velocity is independent of the number of qubits but is larger for higher k Renyi entropies. The size of the linear range L_l and the beginning of the plateau at L_s are dependent on the number of qubits. L_l is contained in region A and L_s specifies the range where optimization does not work effectively. The value of the entanglement entropy at the plateau (3.6) satisfies the volume law up to a numerical shift that depends on k .

the root-mean-square deviation for $0 \leq L \leq n/2$, i.e. ³

$$L_l = \max \left\{ L : |\mathcal{R}_A^k(L) - v_k L| \leq 2\sqrt{\frac{2}{n+2} \sum_{\ell=0}^{n/2} (\mathcal{R}_A^k(\ell) - v_k \ell)^2} \right\}. \quad (3.5)$$

The estimated values of L_l , computed at different n and k , are collected in the fourth column of Table 1. They suggest that the linear growth region tends to expand as the entropy order k increases.

At a late time, Figures 3–5 show that the Renyi entropy \mathcal{R}_A^k saturates to a constant $r_{n,k}$ for any n and k . We can estimate the value $r_{n,k}$ of the plateau by taking the temporal average over entropies within a time frame of $200 \leq L \leq 250$. The estimated values of $r_{n,k}$ are listed in the fifth column of Table 1. They exhibit a simple dependence on $n_A = n/2$:

$$\mathcal{R}_A^k(\rho_A) = r_{n,k} \simeq n/2 - c_k = \text{Vol}(A) - c_k, \quad (3.6)$$

which provides evidence for the volume law scaling of the late-time Renyi entropies [6]. The numerical shift $c_k > 0$ is larger for higher-order k Renyi entropies which is consistent with their monotonic decrease. Let us estimate the layer L_s that is the lower bound of the plateau region. We define it phenomenologically as the layer L where the deviation $|\mathcal{R}_A^k(L) - r_{n,k}|$ between the circuit entropy and the constant becomes smaller than two times the root-mean-square deviation for $200 \leq L \leq 250$, i.e.

$$L_s = \min \left\{ L : |\mathcal{R}_A^k(L) - r_{n,k}| \leq 2\sqrt{\frac{1}{51} \sum_{\ell=200}^{250} (\mathcal{R}_A^k(\ell) - r_{n,k})^2} \right\}. \quad (3.7)$$

³The coefficient 2 in (3.5) is chosen phenomenologically in our case in order to be compatible with the numerical data.

The estimated values of L_s , computed at different n and k , are summarized in the sixth column of Table 1. Note that $L_s \sim \mathcal{O}(n)$ simply because

$$L_s \gtrsim \frac{\text{Vol}(A) - c_k}{v_k \cdot \text{Area}(\partial A)} \sim \frac{n_A}{v_k} \sim \mathcal{O}(n). \quad (3.8)$$

Such linear scaling is consistent with the argument that a unitary design that maximizes all Renyi entropies can be reached in time scale linear in n [6].

Our analysis shows that at least for finite n there is a gap between L_l and L_s , corresponding to the transient region. Details of the entanglement curves in this crossover region are largely model-dependent (see [21] for an example).

4 Hamiltonians

We described the entanglement/proximity diagnostic for random circuit states before optimization, under the assumption that the ground state of the optimization problem follows the area law of the entanglement. It is essential for efficient optimization that the ground state is not a generic quantum state as are our randomly sampled pre-optimization states diagnosed by several entanglement entropies. Evidently, the ground state's entanglement scaling depends on the Hamiltonian. We will consider the three one-dimensional Hamiltonian systems in this paper: the nearest-neighbor and the long-range Ising models coupled to a transverse magnetic field and the Sachdev-Ye-Kitaev model [11–13]. Here we summarize some important characteristics of their ground states. We will see that while the two Ising Hamiltonians have as their ground states low-entangled states, the SYK ground state follows the volume law scaling of the entanglement [14]. The detrimental effect of the volume law entanglement in the gradient-based optimization will be shown in the next section, displaying the strength of the entanglement diagnostics.

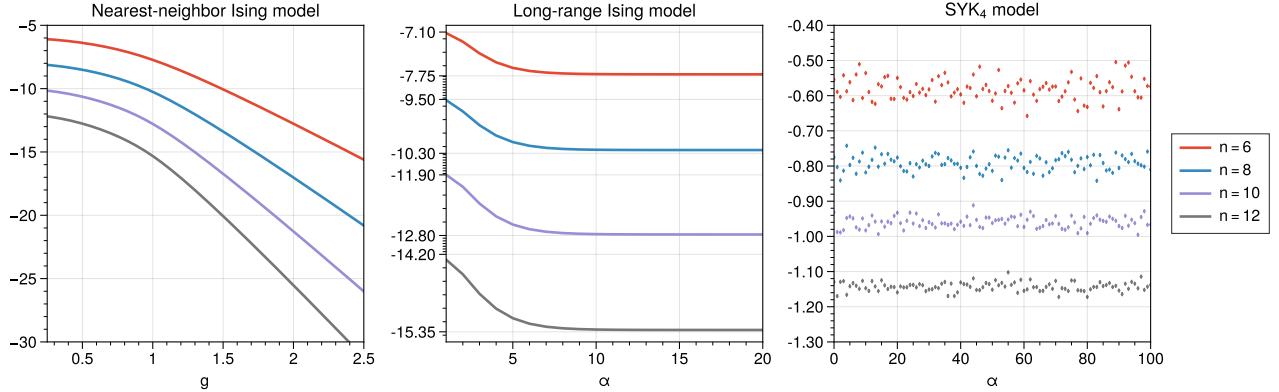


Figure 7: Left: The ground state energies of the nearest-neighbor transverse-field Ising Hamiltonian as a function of the magnetic field strength g for different numbers of spin variables n . When $g = 0$ the ground state energy is $-n$ corresponding to periodically aligned "spin up, spin down" in the \hat{z} direction. As g increases the second term in (4.1) dominates and the ground state energy is approximately $-gn$ corresponding to all spins aligned in $-\hat{x}$ direction. Middle: The ground state energies of the long-range transverse-field Ising Hamiltonian for different numbers of spin variables n as a function of the interaction strength α with a magnetic field strength $g = 1$. At $\alpha \simeq 10$ we see a plateau corresponding to the nearest-neighbors transverse-field Ising ground state. Right: The ground state energies of the SYK model as a function of a random seed for different system size n . The energies are high in comparison to the two Ising models.

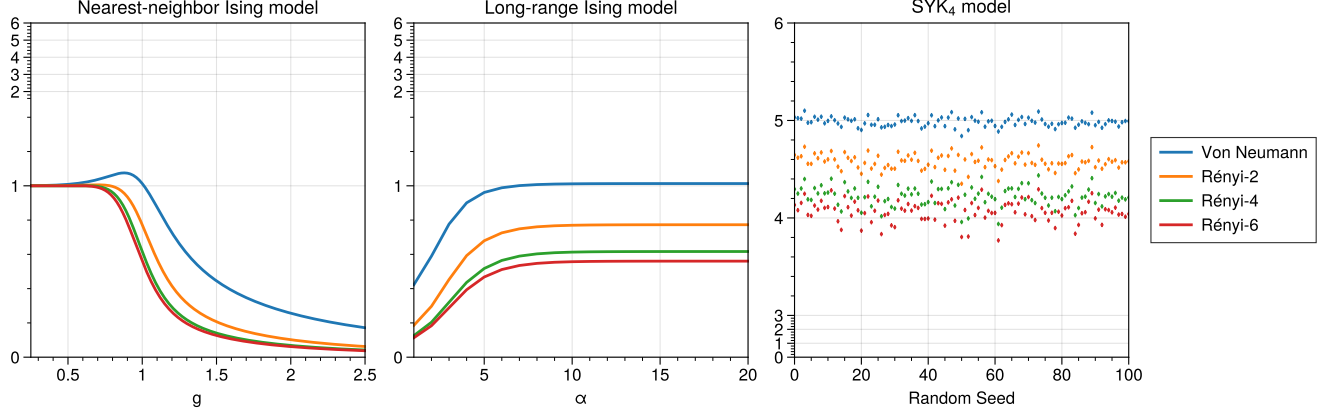


Figure 8: Left: Various Renyi entropies of the ground state of the nearest-neighbor transverse-field Ising model as a function of g for $n = 12$ spin variables. Middle: Various Renyi entropies of the ground state of the long-range transverse-field Ising model as a function of α when $g = 1$ for $n = 12$ spin variables. For both Ising models, the entropies of the ground states are near those of the circuit states in region *A*. Right: Various Renyi entropies of the ground state of the SYK model as a function of a random seed for $n = 12$ spin variables. The entropies are high and relatively close to the maximal entropy, 6 in this case. They are close to those of the circuit states in regions *B*, *C*.

4.1 The Nearest-Neighbours Transverse-Field Ising Model

The one-dimensional Ising Hamiltonian with a nearest-neighbor interaction coupled to a transverse magnetic field is:

$$H = \sum_{i=1}^n \sigma_{z,i} \sigma_{z,i+1} + g \sum_{i=1}^n \sigma_{x,i} , \quad (4.1)$$

where we impose the periodic boundary condition, i.e., $i \sim i + n$. We denoted the Pauli- x/z matrix acting on the i 'th qubit by $\sigma_{x,i}/\sigma_{z,i}$, respectively. The coupling to the transverse magnetic field satisfies $g > 0$.

This model is exactly solvable and its ground-level energy reads [22]:

$$E_g = - \sum_{k=0}^{n-1} \left(1 + g^2 - 2g \cos \left(\frac{2\pi k}{n} \right) \right)^{1/2} . \quad (4.2)$$

In the absence of the magnetic coupling, i.e., $g = 0$, the ground state is in the anti-ferromagnetic phase where all spin variables are aligned antiparallel to the neighboring spins in the z direction, leading to the ground energy $E_0 = -n$. The spin-field coupling in (4.1) gradually contributes more significantly to E_g as the magnetic field strengthens. When g reaches the critical value g_c , the spin-field coupling in (4.1) starts to dominate over the spin-spin interaction, implying a quantum phase transition to the paramagnetism where all spins align in $-x$ direction. For $g \gg g_c$, the ground state energy is approximately $E_g \simeq -gn$.

In Figure 7 we plot the ground energy (4.2) for different numbers of spin variables n as a function of the coupling $0 \leq g \leq 2.5$. Various Renyi entropies of the ground state for $n = 12$ are plotted in Figure 8. The second Renyi entropy for all energy eigenstates of the $n = 12$ system is plotted in Figure 9.

4.2 The Long Range Transverse-Field Ising Model

In the long-range extension of the antiferromagnetic Ising model one adds long-range interactions that follow a power-law decay with the distance. The Hamiltonian reads:

$$H = \sum_{i < j} \frac{1}{d(i,j)^\alpha} \sigma_{z,i} \sigma_{z,j} + g \sum_{i=1}^n \sigma_{x,i} \quad (4.3)$$

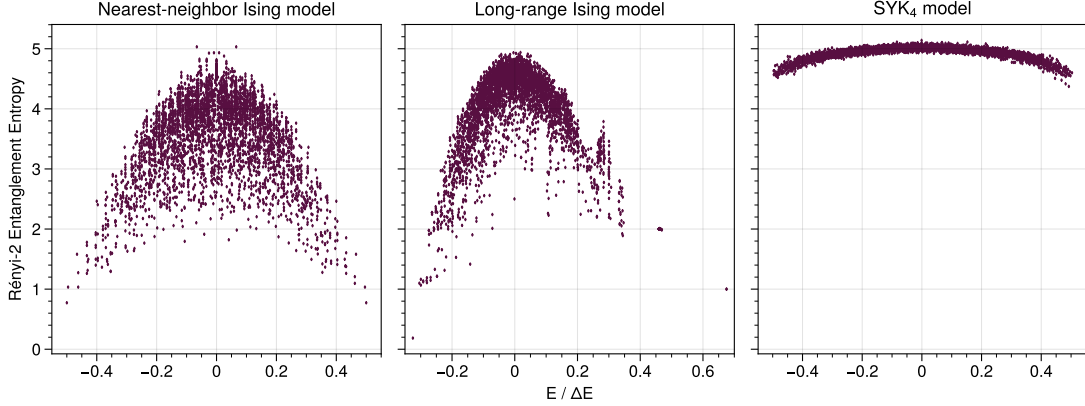


Figure 9: Left: The second Rényi entropy of all energy eigenstates of the nearest-neighbor transverse-field Ising model at $g = 1$. The horizontal axis represents the energy eigenvalue divided by the bandwidth. Middle: The second Rényi entropy of the eigenstates of the long-range transverse-field Ising model at $g = \alpha = 1$. The ground state entropy is lower than that of the nearest-neighbor model. Right: The second Rényi entropy of the eigenstates of the SYK model at a particular random seed, used in Section 5.2. Their entropies are all high and close to each other.

where $d(i, j)$ is the shortest distance between the i 'th and j 'th spin variables under the periodic boundary condition $i \sim i + n$. The long-range spin couplings vanish in the limit when the decay exponent goes to positive infinity $\alpha \rightarrow \infty$ and the Hamiltonian (4.3) reduces to (4.1).

As with the nearest-neighbor Ising model (4.1), the long-range Ising model (4.3) exhibits a quantum phase transition between the anti-ferromagnetic and paramagnetic phases for any value of α . In addition, it was found in [23] that the anti-ferromagnetic ground state can have entanglement entropy that grows with the system size thus violating the area law. The entanglement entropy's scaling behavior is either logarithmic ($\alpha > 1$) or sub-logarithmic ($\alpha < 1$) in the system size (number of spin states n). The MPS (matrix product state) ansatz can still well-approximate the ground state [23, 24], thus we expect that this mild violation of the area law entanglement is not an obstacle for the gradient-based optimization even for large n .

Figure 7 displays the ground state energy of the Hamiltonian (4.3) as a function of the interaction strength $0 \leq \alpha \leq 20$ in the system of n spin states with the magnetic field strength $g = 1$. The influence of the long-range interactions is almost negligible around $\alpha \simeq 10$, returning to the ground-level energy (4.2) of the nearest-neighbor Ising model. In Figure 8 we plot various Rényi entropies of the long-range Ising ground state for $n = 12$ as a function of α , and the second Rényi entropy for all energy eigenstates of the system in Figure 9. As in the nearest-neighbor Ising case, we see that while the ground state is entangled, its Rényi entropies are far from those of generic states.

4.3 The SYK Model

The Sachdev-Ye-Kitaev (SYK) model [11, 12] consists of random, long-range, all-to-all interactions of qubits, which correspond to the following random couplings of q Majorana fermions:

$$H = (i)^{q/2} \sum_{1 \leq i_1 < \dots < i_q \leq 2n} J_{i_1 \dots i_q} \gamma_{i_1} \dots \gamma_{i_q}, \quad (4.4)$$

where the Majorana fermions $\{\gamma_i\}_{1 \leq i \leq 2n}$ satisfy the Clifford algebra $\{\gamma_i, \gamma_j\} = \delta_{ij}$ and can be translated to the spin variables via the Jorgan-Wigner map. The coupling constants $J_{i_1 \dots i_q}$ are randomly drawn from the Gaussian distribution with mean 0 and variance $(q-1)!/(2n)^{q-1}$. Much attention has been paid to the SYK model because it is exactly solvable and simultaneously exhibits a chaotic dynamics for $q \geq 4$ [12, 13].

We will consider the $q = 4$ case and refer to SYK_4 as the SYK model. Each random draw of the coupling constants $J_{i_1 \dots i_4}$ from the Gaussian distribution defines a different SYK model. In Figure 7 we display the

ground state energy of the Hamiltonian (4.4) for 100 individual SYK instances with n qubits, or equivalently, with $2n$ Majorana fermions. The corresponding values of the ground state entanglement entropies when $n = 12$ are depicted in Figure 8, showing that the SYK ground states are much more entangled than the Ising models ground states [14]. More generally, all the eigenstates of the SYK Hamiltonian (4.4) possess entanglement entropies that follow a volume-law scaling [14] as seen in Figure 9 where the Renyi-2 entropy is plotted for the entire spectrum of a particular SYK model when $n = 12$. One can also see in Figure 9 that the spectral gap, i.e., the difference between the ground state and first-excited energy levels, of the SYK model is smaller than that of the Ising models, and the density of states near the ground state is higher.

4.4 Information Inequality

Let us draw the inequality (2.8) in Figure 10, i.e.,

$$\frac{|\text{Tr}(\rho_{g,A}^k) - \text{Tr}(\rho_{c,A}^k)|}{\Delta} \leq 2k \quad (4.5)$$

at $k = 2$ and 4 , where $\Delta = \frac{1}{2}\|\rho_{g,A} - \rho_{c,A}\|_1$ is the trace distance between the reduced density matrices. It is drawn for $n = 12$ qubits, based on the sample average over 50 random circuits, with respect to the three Hamiltonian systems that we consider, i.e. the two transverse-field Ising models and the SYK model.

The entanglement spectra of the Ising models' ground states is close to that of the circuit states within the region A of Figure 2, while that of the SYK ground state is close to that of the circuit states within the regions B and C . Since the trace distance between the ground states and the circuit states is not as close, we see that the LHS of (4.5) is small for Ising models when the circuit state is in region A while it is small for the SYK model when the circuit state is in regions B and C . We will see, however, that unlike the Ising models, it is difficult to optimize the energy cost function of the SYK model. This is because there are many states with entanglement structure similar to that of the SYK ground state, yet having very different energies.

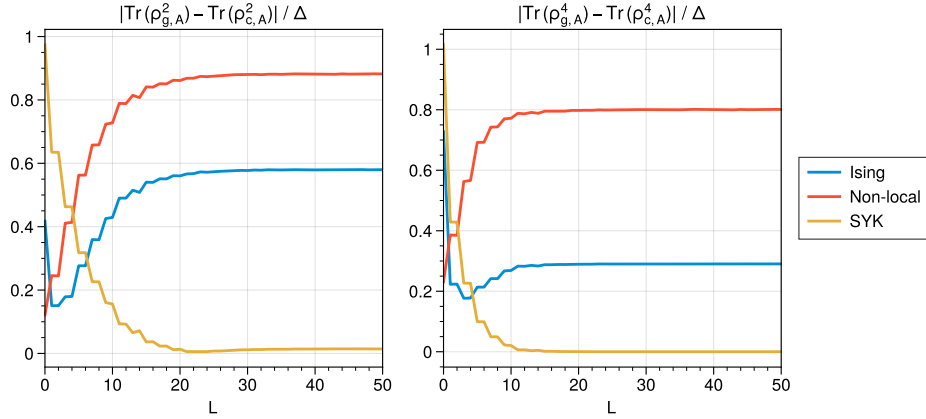


Figure 10: The LHS of the inequality (4.5) for the three different Hamiltonian systems with $n = 12$ qubits, averaged over 50 random circuits, whose parameters are drawn from the uniform distribution $\mathcal{U}(0, 2\pi)$.

5 Optimization

In this section we consider the classical part of the hybrid quantum/classical algorithm. The objective is to find a circuit parameter θ^* that can closely approximate the ground state energy, $E(\theta^*) \simeq E_g$, by taking

iterative steps proportional to the negative gradient of the energy function (2.1) at each point:

$$\theta_{\tau+1} = \theta_{\tau} - \eta \nabla E(\theta_{\tau}). \quad (5.1)$$

The iteration begins with an output state $\rho_c(\theta_{in})$ of the quantum circuit at an initial parameter θ_{in} drawn from the uniform distribution $\mathcal{U}(0, 2\pi)$. The readout of the circuit state is done by repeated measurements of the Pauli string operators that serve as the basis of Hermitian operators. The measurement outcome is relayed to the classical device to evaluate the cost function $E(\theta_{in})$. Since circuit wavefunctions will only be constructed on a classical simulator throughout this paper, the readout and accompanying noise will not be taken into account. The parameter update (5.1) requires knowing the energy gradient at $\theta = \theta_{in}$, which can be estimated by executing the original circuit at shifted gate parameters [25]. At an updated value θ_1 of the circuit parameter, the quantum circuit operates to create a new wavefunction $\rho_c(\theta_1)$, which will be repeatedly measured to estimate the corresponding energy $E(\theta_1)$ and gradient $\nabla E(\theta_{in})$ for the next iteration. By iterating this process, we will reach a parameter value θ_f that leads to a quantum state $\rho_c(\theta_f)$ having as low mean energy $E(\theta_f)$ as possible. If there are no obstacles, we expect to reach the ground level energy eventually. We will choose the termination condition for the iteration as updating the circuit parameter 10^4 times and thus waiting sufficient time for convergence, i.e., $\theta_f = \theta_{10000}$.

The learning rate η is a hyperparameter that determines the step size taken in the parameter space at each update. We recall the following obstacles in choosing the learning rate η : A too-large learning rate will cause overshooting near the minimum energy point, while a too-small learning rate will make the optimization stuck at local minima. We will put aside some well-known convergence techniques, e.g., learning rate scheduling or adaptive learning rate methods, and stick to a vanilla gradient descent with $\eta = 0.005$ for all the numerical experiments in this paper. In particular, at a late time when the parameter update is not too large, each step of the gradient descent will modify the mean energy simply as:

$$\Delta E(\theta_{\tau}) \equiv E(\theta_{\tau+1}) - E(\theta_{\tau}) = -\eta \|\nabla E(\theta_{\tau})\|_2^2. \quad (5.2)$$

We will see the difficulty in generating a successful optimization trajectory that starts/ends at a quantum state close to generic states, that are the majority of the Hilbert space states, unless being equipped with an exponentially large parameter space. Our intuition is based on measuring the evolution of the entanglement entropies (1.3) and (1.4) along the optimization trajectory, rather than a more commonly-used metric, e.g., the trace distance between the circuit state and the target state.

Consider a partitioning of the Hilbert space into three subsets characterized by their entanglement entropies, say A , B , C , in accordance with Figure 2. Generic quantum states lie in the region C , as their entanglement entropies are close to the maximum. When the target state is a non-generic state that resides in the region A , i.e., following the area-law scaling of the entanglement entropy, the entanglement entropy tends to decrease along the optimization trajectory. However, we will observe that if an initial state $\rho_c(\theta_{in})$ belongs to the region B or C , the gradient descent update (5.1) is unable to cross over to the region A and is stuck at an intermediate local minimum thus failing to reach the ground-level energy E_g . We will illustrate it with the Ising models' ground states in Section 5.1. Another interesting case, which will be discussed in Section 5.2, is when the target state itself is highly entangled and belongs to the region C . The entanglement entropy of the circuit state $\rho_c(\theta_{\tau})$ still tends to decrease on average. In the case that the initial circuit state has a smaller entanglement entropy than the target state, i.e., $\mathcal{R}_A^k(\rho_{c,A}) < \mathcal{R}_A^k(\rho_{g,A})$, the optimization enlarges their gap. When $\mathcal{R}_A^k(\rho_{c,A}) > \mathcal{R}_A^k(\rho_{g,A})$, the optimization moves toward reducing the gap on average. However, as in the Ising models cases, it stops without narrowing the gap completely being unable to cross over to the region that supports the desired degree of entanglement. To summarize, all our results indicate the following: the Hilbert space can be partitioned to multiple layers distinguished by the amount of the bipartite entanglement entropy. Moving across distant layers via the gradient descent (5.1) of the energy function $E(\theta)$ is a very demanding task, which generically requires an exponentially large parameter space [7].

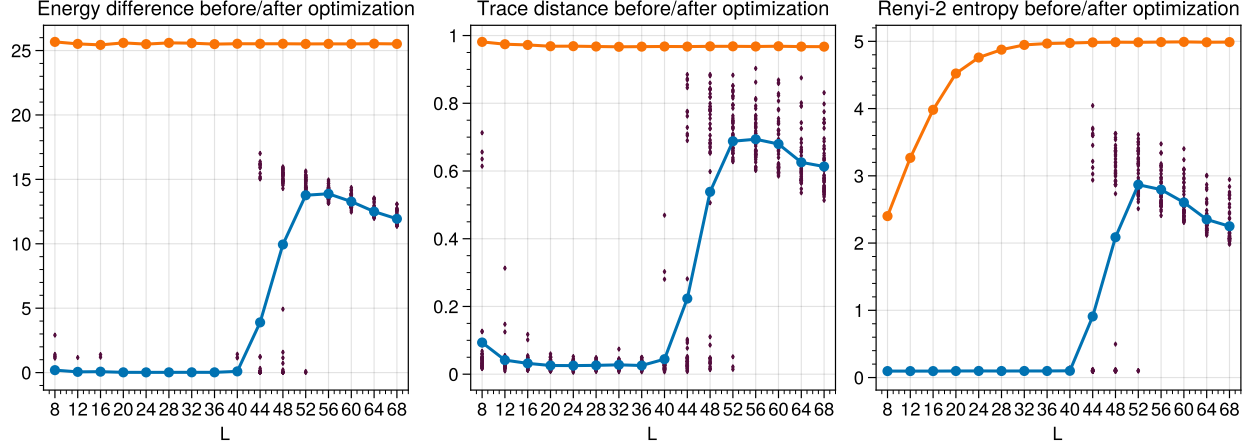


Figure 11: The optimization to reach the nearest-neighbours transverse-field Ising model at $g = 2$ as a function of the number of circuit layers. Left: The difference between the circuit state and the ground state energy before and after the optimization. We see that optimization works very well for circuit states in the region A . Middle: The trace distance between circuit state and the ground state before and after the optimization. Right: The Renyi entropy of the circuit state before and after optimization. We see that the trace distance and entropy diagnostic are both correlated with the minimized variational energy.

5.1 The Transverse-Field Ising Models

Let us discuss the optimization outcome of the variational circuit via the energy gradient descent (5.1) of the Ising Hamiltonians (4.1) and (4.3) coupled to the transverse magnetic field. In Figures 11–13, we summarize the results as a function of the number of circuit layers L . The orange/blue curves in all panels represent a certain quantity before/after the optimization.

In Figure 11, we draw the optimization results for the nearest-neighbor Ising model (4.1) coupled to the transverse field at $g = 2$. The left panel shows the energy difference $E(\theta) - E_g$ between the circuit state (2.1) and the exact ground state (4.2). The middle panel depicts the trace distance $\frac{1}{2}\|\rho_{c,A} - \rho_{g,A}\|_1$ between the reduced circuit state and the reduced ground state. The right panel represents the Renyi-2 entropy (1.3) of the circuit state. We find that the optimization works very well for the circuits with $L \lesssim 40$. Besides, we observe that variational circuits within an intermediate depth of $40 \lesssim L \lesssim 52$, which correspond to the region B of Figure 2, may or may not reach the ground state energy, showing the transition from the region A to C . All three quantities clearly show the advantage of the quantum circuits that belong to the region A of Figure 2, whose pre-optimization entanglement entropy is low. Especially, the trace distance and Renyi entropy curves share similar ups-and-downs, showing two diagnostics are correlated.

For comparison, we consider the same Ising model at $g = 1$, where the two terms in the Ising Hamiltonian (4.1) are of the same strength. The optimization results are depicted in Figure 12, consisting of the three panes as before, which express the energy difference, the trace distance $\frac{1}{2}\|\rho_c - \rho_g\|_1$ between the circuit and exact ground states, and the Renyi-2 entropy. Again, the left panel shows that the optimization works successfully as long as $L \lesssim 40$, showing the advantage of the low-entangling region A . A noticeable difference appear in the middle curve for the trace distance, which fails to close the gap despite having approached the ground-level energy closely. Such distinction from the $g = 2$ curve stems from the fact that the entanglement entropy of the $g = 1$ ground state is slightly higher than that of the $g = 2$ ground state, as shown in Figure 8, being a tiny step closer to the region B or C of Figure 2. This shows that the trace distance is very sensitive to small deviations from the ground state energy, decreasing its usefulness as a diagnostic of the accuracy of the circuit approximation. In contrast, the entropy diagnostic remains well-correlated with the energy gap.

In Figure 13, we display the optimization results to reach the ground state of the long-range Ising model coupled to the transverse field at $\alpha = g = 1$ for a range of L . Once again, the high precision approximation

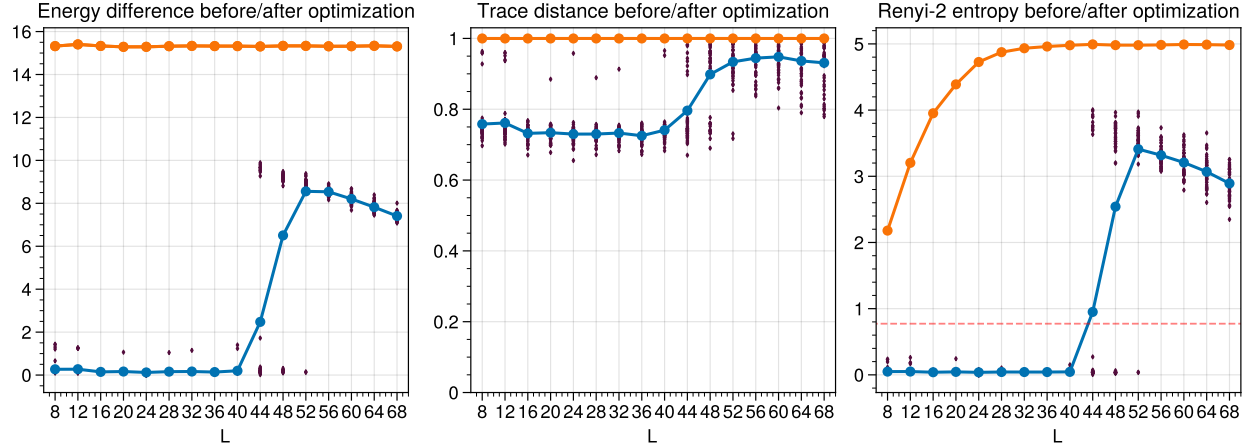


Figure 12: The optimization to reach the nearest-neighbours transverse-field Ising model ground state at $g = 1$ as a function of the number of circuit layers. In the $g = 1$ case the two terms in the Ising Hamiltonian (4.1) are of the same strength. Left: The difference between the circuit state and the ground state energy before and after the optimization. As in the $g = 2$ case, the optimization works very well for circuit states whose L lies within the range A of Figure 2. Middle: The trace distance between the circuit state and the ground state before and after the optimization. Compared to the $g = 2$ case, the trace distance is not small even when the minimized circuit energy approaches the exact ground energy with a small margin of error, showing how sensitive it is to energy deviations. Right: The Renyi entropy of the circuit state before and after optimization. The dashed line denotes the value of the ground state Renyi entropy. The entropy diagnostic is well-correlated with the success of the energy minimization.

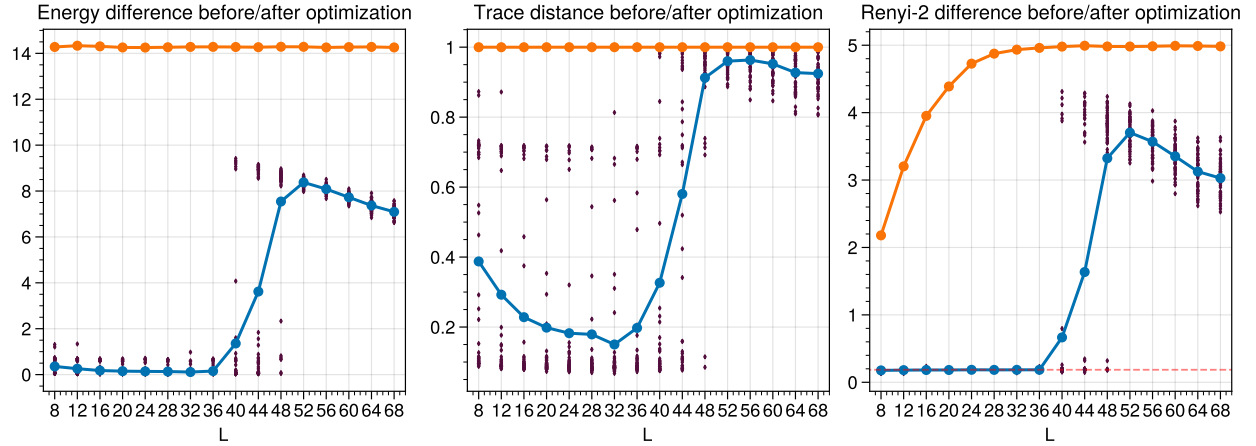


Figure 13: The optimization to reach the ground state of the long-range transverse-field Ising model at $\alpha = 1, g = 1$ as a function of the number of circuit layers. Left: The difference between the circuit state and the ground state energy before and after the optimization. Optimization works well for the circuit states whose L belongs to region A of Figure 2, but the optimal part within the region A is a little shorter than that of Figure 12. Middle: The trace distance between circuit state and the ground state before and after the optimization. We see that the trace distance is sensitive to small deviations from zero of the energy cost function. Right: The Renyi entropy of the circuit state before and after optimization. The dashed line denotes the value of the ground state Renyi entropy.

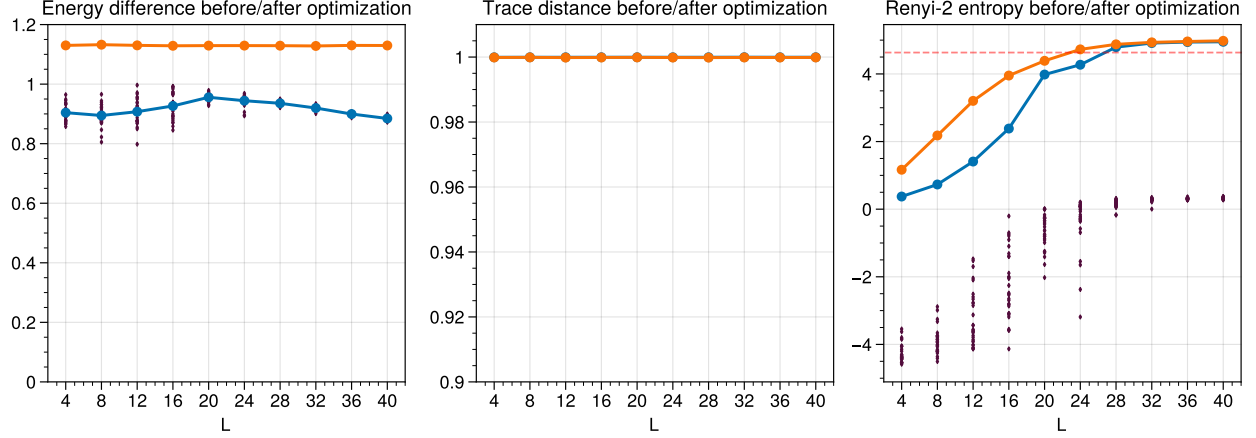


Figure 14: Left: The energy difference between the circuit state and the SYK ground state at different values of L for $n = 12$ qubits. Middle: The trace distance between the circuit state and the ground state. Right: The Renyi-2 entropy of the circuit state. The dashed line denotes the Renyi entropy of the ground state. All three quantities before/after the optimization are expressed by the orange/blue curves, respectively. The two lines for the trace distance are completely overlapping. The circuit optimization fails to reach the ground energy for all $4 \leq L \leq 40$.

of the ground state energy for $L \lesssim 36$ highlights the importance of preparing an initial circuit state to be in the region A of Figure 2. The average trace distance looks more similar to that of Figure 11 rather than Figure 12. The reason is that the entanglement entropy of the long-range Ising ground state at $\alpha = g = 1$ is slightly lower than that of the nearest-neighbor Ising ground state at $g = 1$, while higher than that of the nearest-neighbor Ising ground state at $g = 2$. As mentioned above, the trace distance is very sensitive to small deviations in the energy difference. Instead, the Renyi entropy curve is apparently more well-connected with the success of the variational circuit optimization, hence providing a more reliable diagnostic.

5.2 The SYK Model

We now optimize the variational circuit to approximate the ground state energy E_g of a particular instance of the SYK₄ Hamiltonian. Recall that the entanglement entropy of the SYK₄ ground state is near-maximal and exhibits the volume-law scaling [14]. Since the approximation target state itself behaves like generic quantum states, the given optimization task is now to develop a parameter trajectory that ends at the ground state close to the region B or C of Figure 2. Therefore, unlike the case of approximating the Ising ground energy, choosing an initial circuit from the region A of Figure 2 does not ensure a success of the optimization. Figure 14 summarizes the energy difference and trace distance between the circuit state and the exact ground state, as well as the Renyi-2 entropy of the circuit state, at different values of L . All three quantities before/after the optimization are expressed by the orange/blue curves, respectively. The circuit optimization has failed to reach the ground-level energy for all $4 \leq L \leq 40$.

5.3 Entropy Diagnostic and Optimization

It is informative to look at Figure 15 where we plot the evolution of the second Renyi entropy $\mathcal{R}_A^2(\rho_{c,A}(\theta_\tau))$ as a function of τ , the optimization parameter update step. The dashed line is the Renyi entropy of the ground state. We recall that the Renyi entropies of the Ising models' ground states are relatively low and scaling as the area law, while that of the SYK model's ground state is high and scaling as the volume law.

We see that the $L = 12$ circuit state that belongs to the region A can successfully reach the vicinity of the Ising models' ground states in terms of their Renyi entropies. However, for the $L = 40$ or 68 circuit states which belong to the respective regions B and C , the gradient descent optimization becomes much harder

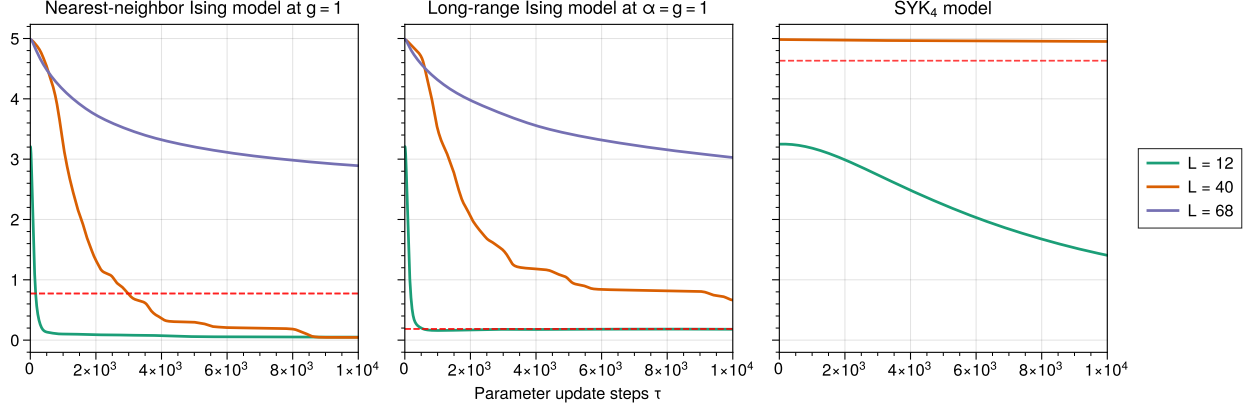


Figure 15: The evolution of the second Renyi entropy as a function of the optimization parameter update step τ for $n = 12$ qubits. The dashed lines denote the values of the ground states' Renyi entropies. Left and Middle: The $L = 12$ circuit state that belongs to the region A can successfully reach the vicinity of the Ising models' ground states in terms of their Renyi entropies. On the other hand, the $L = 40$ circuit state requires a much longer optimization time, and the $L = 68$ circuit state fails to approach the ground states' Renyi entropy. Right: The Renyi entropy decreases in general along the optimization trajectory. Even though the circuit states that lie in regions B and C are close in their entropies to the SYK ground state, it is not sufficient for a successful optimization.

due to their higher Renyi entropies; It either fails (for the circuit within the region C) or take a much longer optimization time (for the circuit within the region B .)

Interestingly, we see that the Renyi entropy decreases in general along the optimization trajectory. In the case of the SYK model, when the initial state is chosen from the range $4 \leq L \leq 24$ with entanglement entropy that is lower than that of the ground state, the parameter update (5.1) enlarges the entanglement gap from the ground state. Above $L = 24$ layers, while the optimization reduces the Renyi entropy difference on average it cannot reach the vicinity of the ground states entanglement entropies. Although the SYK ground state's Renyi entropy is high and close to the entropies of those circuit states in the regions B and C of Figure 2, minimizing the circuit energy fails to reach the ground energy. In general, one needs a higher-dimensional parameter space in order to develop an optimization trajectory that can cross from a region of high entanglement to a region with low entanglement. Especially for the SYK model, an exponentially high-dimensional parameter space is needed to approximate its ground-level energy with high precision [7].

6 Random Graph Circuit Architecture

We have seen the importance of choosing the variational circuit to stay in the low-entangling region of the Hilbert space for the effective minimization of the energy cost function towards the ground state that supports the area-law entanglement entropy. Since the entanglement growth of the random quantum circuit with respect to the discrete time depends on the circuit architecture, certain architectures can be more suitable for solving specific optimization problems than others. A question of much importance is then to identify and quantify better circuit architectures for a given task. For instance, it brings greater efficiency to use a variational circuit that respects some known physical properties, such as the ground state symmetry, to approximate a specific Hamiltonian system [26, 27]. To solve more generic tasks, one may view the quantum circuit as a directed graph whose nodes and links are the qubits and 2-qubit gates, respectively, and consider various circuit architectures [28]. Even though real-world technological considerations may restrict some graph architectures, many feasible options have been largely unexplored yet. In this section, we will make a first step in exploring how entanglement diagnostics and energy optimization depend on the circuit architecture by considering a simple stochastic variation of Figure 1.

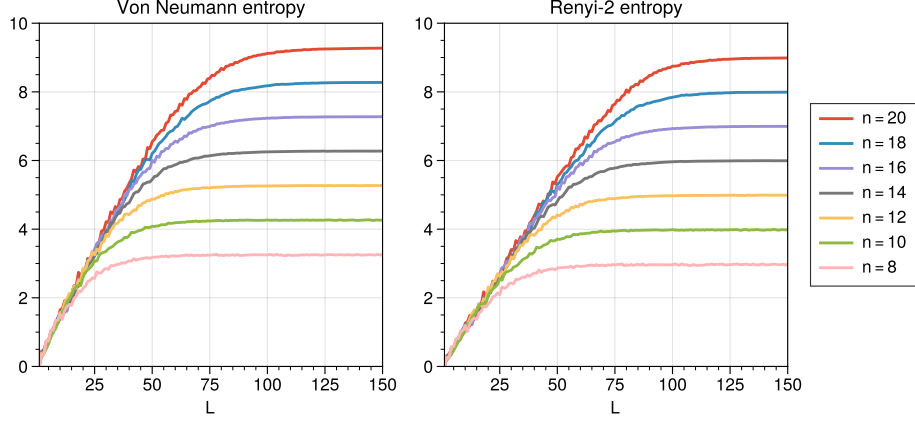


Figure 16: Von Neumann and Renyi-2 entropies averaged over 50 random circuits, whose parameters are drawn from the uniform distribution $\mathcal{U}(0, 2\pi)$ and controlled- Z gates are omitted with probability 0.5.

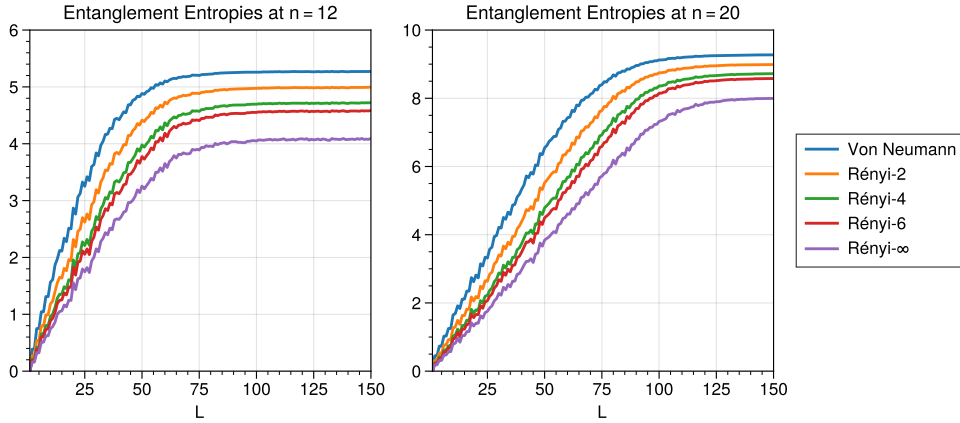


Figure 17: Various entanglement entropies averaged over 50 random circuits, whose parameters are drawn from the uniform distribution $\mathcal{U}(0, 2\pi)$ and controlled- Z gates are omitted with probability 0.5.

6.1 Circuit Entanglement

Let us consider the variational circuit ansatz, whose architecture is the same as in Figure 1a but omits the CZ entangler (3.2) in the two-qubit gate of Figure 1b with a probability of $p = 1/2$. Since the average number of the entangler is cut in half, we expect that the entanglement growth rate would be halved. Accordingly, the discrete-time to reach the saturation of the entanglement entropy would be doubled.

In Figures 16, 17, and 18, we draw the discrete-time evolution of various entanglement diagnostics under the random circuits with omitting probability $p = \frac{1}{2}$ of the CZ operators, averaged over 50 samples. The overall shape of the curves remains the same as Figures 3–5, but it takes a longer discrete-time L to reach the plateau. They indeed show that generating a state with the same amount of entanglement entropies takes about twice the discrete-time L with the $p = \frac{1}{2}$ circuit, compared to the previous $p = 1$ case, as expected. Similarly, Figure 18 shows the geometric measure of entanglement (1.5) for the $p = \frac{1}{2}$ random circuit, which is the shortest distance from n -qubit product states. We find that, compared to the $p = 1$ curve in Figure 6, it roughly takes twice as many circuit layers to have the same value of the geometric measure.

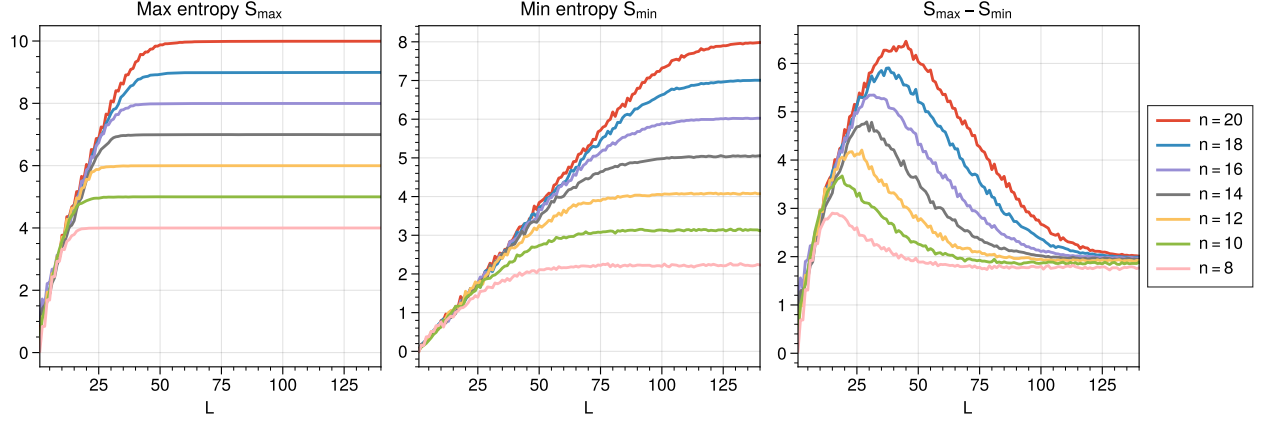


Figure 18: The sample mean of S_{\max} , S_{\min} , $S_{\max} - S_{\min}$ over 50 instances of random circuits, whose parameters are drawn from the uniform distribution $\mathcal{U}(0, 2\pi)$ and controlled-Z gates are omitted with probability 0.5.

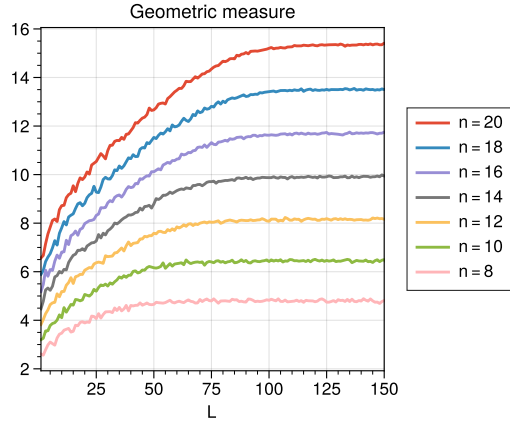


Figure 19: The Geometric measure of entanglement (1.5) averaged over 50 random circuits, whose parameters are drawn from the uniform distribution $\mathcal{U}(0, 2\pi)$ and controlled-Z gates are omitted with probability 0.5.

6.2 Optimization

We turn to the optimization results of the $p = 1/2$ variational circuit towards the ground state of the nearest-neighbor Ising model (4.1) at $g = 1$ as a function of the circuit depth L . They are all summarized in Figure 20. The energy difference and the trace distance between the circuit state and the exact ground state are depicted in the left and middle panels, respectively. The right panel shows the Renyi-2 entropy of the circuit state. The orange/blue curves therein represent each specific quantity of the circuit states before/after optimization. What we observe from Figure 20 is the following: Although the specific values of L that divide the region A , B , C in Figure 2 have changed by introducing the omission probability $p = 1/2$, the optimization still works very well for the variational circuits that lie in the region A . For the circuit states in the region B or C , the trajectory under the gradient descent cannot close the entanglement gap below a certain degree. In all cases, unlike the trace distance, the entropy diagnostic shows an apparent correlation with the successful minimization of the energy cost function (2.1), showing its usefulness regardless of circuit-specific details.

Note, that since the $p = \frac{1}{2}$ circuit reaches the same entanglement structure as the $p = 1$ circuit by doubling the number of layers, its parameter space dimension created by the one-qubit gates is larger by

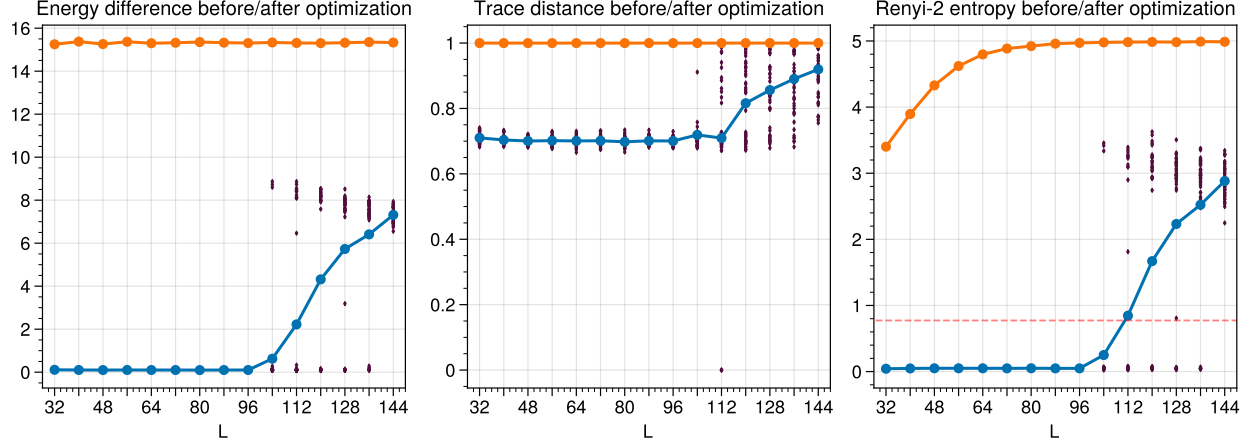


Figure 20: The optimization to reach the nearest-neighbours transverse-field Ising model ground state at $g = 1$ as a function of the number of the $p = \frac{1}{2}$ circuit layers. We see the same pattern as in the optimization of the $p = 1$ circuit in Figure 12 with a delay of about twice the number of layers. Left: The difference between the circuit state and the ground state energy before and after the optimization. The optimization works very well for the circuit ansatzes in the region A. Middle: The trace distance between the circuit state and the ground state before and after the optimization. The trace distance is not small even when the energy minimization goes well. Right: The Renyi-2 entropy of the circuit state. The dashed line denotes the value of the ground state Renyi entropy. Unlike the trace distance, the entropy diagnostic is correlated with the success of the energy cost function optimization.

factor two than that of the $p = 1$ circuit. We checked that this doubling of the parameter space brings a minor positive effect compared to the $p = 1$ circuit on the optimization speed, i.e., in terms of the number of steps needed to reach the ground state energy level.

7 Restricted Circuit Parametrization

When having a larger number of circuit layers in Figure 1, we increase the circuit state entanglement by applying more two-qubit control-Z gates, however, we also simultaneously increase the number of parameters θ on which the circuit state depends because of the larger number of applied one-qubit rotation gates. In this section we would like to separate the two effects and study the dependence of the circuit on a restricted set of parameters. In order to do that we will impose on the parameters of each layer the constraint:

$$\theta_{\ell,1} = \theta_{\ell,2} = \dots = \theta_{\ell,n} \quad \text{for all } 1 \leq \ell \leq L. \quad (7.1)$$

The analysis is complementary to that of section 6, where we restricted the application of the control-Z gates and changed the circuit state entanglement growth as a function of the number of circuit layers but we did not restrict the number of the rotation parameters. In Figure 20 we demonstrated the importance of preparing the initial circuit state within a suitable range of the entanglement entropy of the ground state. Here we will consider the impact of having a high/low-dimensional parameter space while maintaining the same entanglement growth rate. We will see that although the circuit state entanglement is not affected, it can reduce the efficiency of the classical optimization algorithm.

The basic 2-qubit gate \mathcal{O}_2 that we use in the random quantum circuit in Figure 1 reads:

$$\mathcal{O}_2 = CZ_{i,j} \cdot R(\theta_{l,i}) \otimes R(\theta_{l,j}), \quad (7.2)$$

where $CZ = \text{diag}(1, 1, 1, -1)$ and $R(\theta)$ is the Pauli rotation (3.1) around the y -axis. It is curious to note

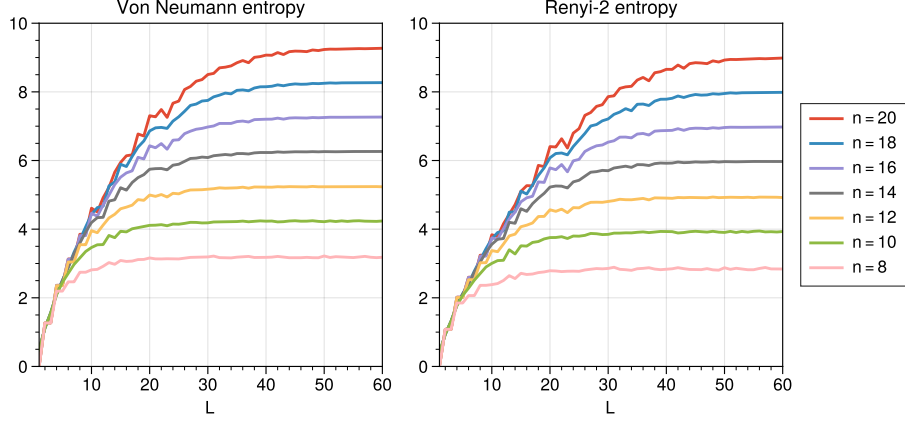


Figure 21: Von Neumann and Renyi-2 entropies averaged over 50 random circuits, whose parameters at an individual layer are equal and randomly drawn from the uniform distribution $\mathcal{U}(0, 2\pi)$, as a function of the number of layers.

that the constraint (7.1) is equivalent to imposing $[\mathcal{O}_2, Q] = 0$ on all 2-qubit pairs that \mathcal{O}_2 acts upon, where:

$$Q = \begin{pmatrix} q_1 + q_2 & 0 & 0 & 0 \\ 0 & q_1 & q_2 & 0 \\ 0 & q_2 & q_1 & 0 \\ 0 & 0 & 0 & q_1 + q_2 \end{pmatrix}. \quad (7.3)$$

Note, however, that Q is not a global symmetry of the circuit because it does not commute with other \mathcal{O}_2 's on the next layer that alternates the odd/even numbering.

7.1 Circuit Entanglement

In Figures 21–23 we summarize the entanglement diagnostics of the random quantum circuit, in Figure 1 when restricted to the constraint (7.1). We see that the curves are more wiggly, their overall growth pattern matches that of Figures 3–5 of the unconstrained circuit. The geometric measure curve plotted in Figure 24 is fluctuating more than its counterpart, Figure 6, and converges to a slightly lower value. This constitutes a comparable level of entanglement diagnostics as that of the unconstrained case as a function of the number of circuit layers L . Thus, the constrained circuit (7.1) provides a useful setting for studying the impact of the parameter space dimension.

7.2 Optimization

We will consider the optimization in the case of the nearest-neighbours transverse-field Ising model at $g = 1$, where the circuit parameters are restricted by (7.1). In Figure 25 (left) we see the difference between the circuit state and the ground state energy before and after the optimization as a function of L . In comparison to the unrestricted circuit, even the variational circuits from the region A do not always give a reliable good approximation of the ground energy. This is also clearly seen by the entanglement diagnostic in Figure 25 (right) which is correlated with the performance of the energy minimization. We see that even with the appropriate structure of entanglement, there is still much importance to the dimension of the parameter space for a successful optimization, and its restriction has a negative effect on the optimization performance.

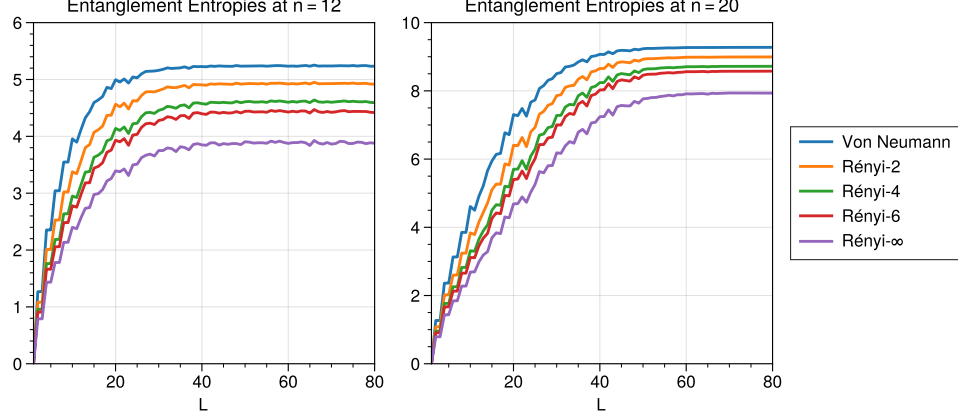


Figure 22: Various entanglement entropies averaged over 50 random circuits, whose parameters at an individual layer are equal and randomly drawn from the uniform distribution $\mathcal{U}(0, 2\pi)$, as a function of the number of layers.

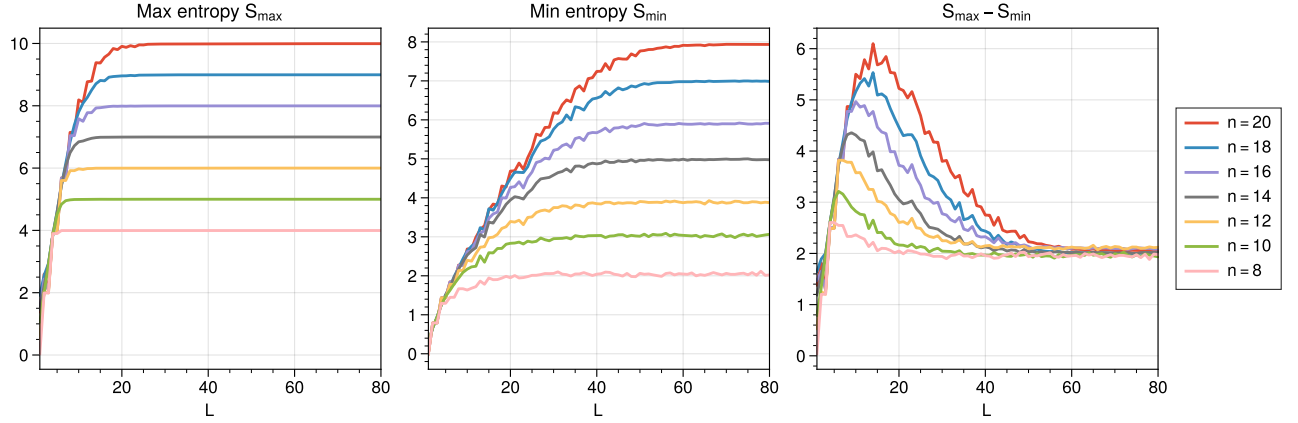


Figure 23: The sample mean of S_{\max} , S_{\min} , $S_{\max} - S_{\min}$ over 50 instances of random circuits, whose circuit parameters at an individual layer are equal and randomly drawn from the uniform distribution $\mathcal{U}(0, 2\pi)$

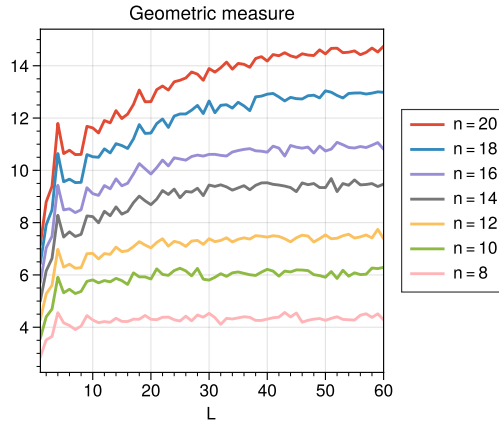


Figure 24: The Geometric measure of entanglement (1.5) averaged over 50 random circuits, whose circuit parameters at an individual layer are equal and randomly drawn from the uniform distribution $\mathcal{U}(0, 2\pi)$

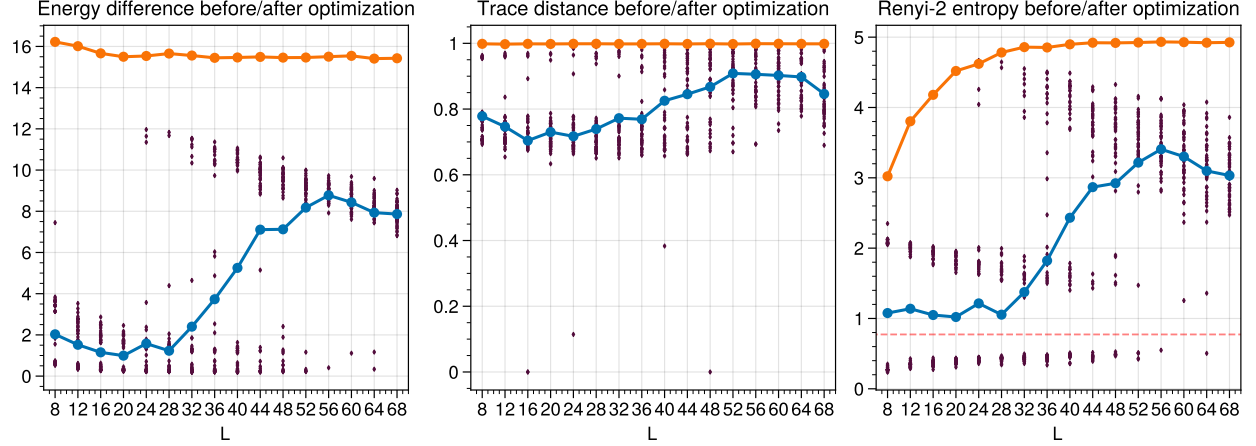


Figure 25: The optimization to reach the nearest-neighbours transverse-field Ising model ground state at $g = 1$ as a function of the circuit depth L , where the circuit parameters are restricted to (7.1). We see the output is not as good as that of the unrestricted circuit. Left: The difference between the circuit state and the ground state energy before and after the optimization. Even the circuits from the region A do not guarantee a reliable approximation of the ground level energy. Middle: The trace distance between the circuit state and the ground state before and after the optimization. Right: The Renyi-2 entropy of the circuit state. The dashed line denotes the value of the ground state Renyi entropy. Unlike the trace distance, the entropy diagnostic is correlated with the performance of the circuit energy minimization.

8 Discussion and Outlook

We considered the random circuit model of quantum computation and studied the problem of minimizing efficiently the energy cost function of a Hamiltonian. We analysed the Renyi entropies as diagnostics for the efficiency of the variational circuit in producing an appropriate quantum state for solving the optimization problem. While entanglement is a valuable non-local resource for quantum computations, we showed that too much entanglement is a hurdle⁴, and we quantified an optimal range of the circuit depth. Thus, having a deep random quantum circuit is not necessarily an advantage.

The random quantum circuit has a characteristic pattern of entanglement growth as a function of the number of circuit layers, which we naturally divided to three parts. We identified a region of entanglement along the linear growth as the optimal region which we denoted by A . Region C is the plateau where a volume law of entanglement holds, and B is the transition region between A and C . The vanishing gradient problem [3–5] is associated with a 2-design structure and may exist only in the regions B and C . We considered the search for the ground state energy of three different Hamiltonians: the transverse-field nearest-neighbors Ising model, the transverse-field long-range Ising model and the SYK chaotic model. We analysed the qualitative and quantitative differences between these Hamiltonians. We demonstrated that the circuit ansatzes that stay in the region A are very effective for the Ising models but not for the SYK model. Regions B and C circuit states are not effective neither for the Ising models nor for the SYK model unless one increases the circuit parameter space exponentially. We also studied a stochastic random circuit where we introduced the control-Z gate only with probability $p = \frac{1}{2}$. We analyzed its entanglement growth and optimization performance. By imposing restrictions on the parameter space of the circuit, we also studied the importance of the parameter space to the optimization performance for a given entanglement structure.

There are various directions one may wish to follow. First, the entanglement curve of the circuit is affected by using different circuit architectures [30]. One can try to find the relationship between the properties of random graphs that encode the circuit architecture and the entanglement diagnostic for efficient optimization, e.g., how the circuit graph affects the entanglement velocity v_E of the linear growth region. It will help to

⁴See also the discussion in [29].

determine an optimal initial circuit state for a given architecture and optimization task. Second, here we have studied one-dimensional systems, and it is desirable to generalize to higher dimensions. Another direction to follow is to study random quantum circuits with diffusive conserved charges [31,32]. On the one hand, a conserved charge slows down the entanglement growth, but on the other hand, it restricts a set of expressible quantum states by the variational circuit. Such a symmetry-preserving circuit could be efficient for optimization problems where the target state is known to respect certain imposed symmetries [26,27]. Fourth, the random quantum circuit is generically a chaotic system. One can take certain probes of the quantum chaos, such as the operator spreading and the spectral form factor of the reduced density matrix, and relate them to the efficiency of the optimization [10]. They are also partially related to the entanglement diagnostics since the evolution of the Renyi 2-entropy can be understood from the operator spreading [33]. Finally, one may wish to introduce noise and investigate how it affects the optimization performance.

Acknowledgements

We would like to thank Khen Cohen, Tom Levy, Eun Gook Moon, Muli Safra and Lior Wolf for valuable discussions. We are grateful to Jaedeok Kim and Dario Rosa for the collaboration at the early stage of this project. The work of J.K. is supported by the NSF grant PHY-1911298 and the Sivian fund. The work of Y.O. is supported in part by Israel Science Foundation Center of Excellence, the IBM Einstein Fellowship and John and Maureen Hendricks Charitable Foundation at the Institute for Advanced Study in Princeton. Our Python code for the numerical experiments is written in TensorFlow Quantum [34]. The experimental data are managed by using Weights & Biases [35].

References

- [1] J. Preskill, “Quantum Computing in the NISQ era and beyond,” *Quantum* **2** (Aug, 2018) 79.
<http://dx.doi.org/10.22331/q-2018-08-06-79>.
- [2] E. Farhi, J. Goldstone, and S. Gutmann, “A Quantum Approximate Optimization Algorithm,”
[arXiv:1411.4028 \[quant-ph\]](https://arxiv.org/abs/1411.4028).
- [3] J. R. McClean, S. Boixo, V. N. Smelyanskiy, R. Babbush, and H. Neven, “Barren plateaus in quantum neural network training landscapes,” *Nature Communications* **9** no. 1, (Nov, 2018) .
<http://dx.doi.org/10.1038/s41467-018-07090-4>.
- [4] M. Cerezo, A. Sone, T. Volkoff, L. Cincio, and P. J. Coles, “Cost-function-dependent barren plateaus in shallow quantum neural networks,” [arXiv:2001.00550 \[quant-ph\]](https://arxiv.org/abs/2001.00550).
- [5] C. O. Marrero, M. Kieferová, and N. Wiebe, “Entanglement induced barren plateaus,”
[arXiv:2010.15968 \[quant-ph\]](https://arxiv.org/abs/2010.15968).
- [6] Z.-W. Liu, S. Lloyd, E. Zhu, and H. Zhu, “Entanglement, quantum randomness, and complexity beyond scrambling,” *Journal of High Energy Physics* **2018** no. 7, (Jul, 2018) .
[http://dx.doi.org/10.1007/JHEP07\(2018\)041](http://dx.doi.org/10.1007/JHEP07(2018)041).
- [7] J. Kim, J. Kim, and D. Rosa, “Universal effectiveness of high-depth circuits in variational eigenproblems,” [arXiv:2010.00157 \[quant-ph\]](https://arxiv.org/abs/2010.00157).
- [8] Z.-W. Liu, S. Lloyd, E. Y. Zhu, and H. Zhu, “Generalized Entanglement Entropies of Quantum Designs,” *Physical Review Letters* **120** no. 13, (Mar, 2018) .
<http://dx.doi.org/10.1103/PhysRevLett.120.130502>.
- [9] T.-C. Wei and P. M. Goldbart, “Geometric measure of entanglement and applications to bipartite and multipartite quantum states,” *Physical Review A* **68** no. 4, (Oct, 2003) .
<http://dx.doi.org/10.1103/PhysRevA.68.042307>.

- [10] J. Kim and Y. Oz, “Quantum Chaos Diagnostics for Efficient Hybrid Computation,” to appear.
- [11] S. Sachdev and J. Ye, “Gapless spin-fluid ground state in a random quantum Heisenberg magnet,” *Physical Review Letters* **70** no. 21, (May, 1993) 3339–3342.
<http://dx.doi.org/10.1103/PhysRevLett.70.3339>.
- [12] A. Kitaev, “A simple model of quantum holography.”
<http://online.kitp.ucsb.edu/online/entangled15/kitaev/> &
<http://online.kitp.ucsb.edu/online/entangled15/kitaev2/> , 2015.
- [13] J. Maldacena and D. Stanford, “Remarks on the Sachdev-Ye-Kitaev model,” *Physical Review D* **94** no. 10, (Nov, 2016) . <http://dx.doi.org/10.1103/PhysRevD.94.106002>.
- [14] Y. Huang and Y. Gu, “Eigenstate entanglement in the Sachdev-Ye-Kitaev model,” *Physical Review D* **100** no. 4, (Aug, 2019) . <http://dx.doi.org/10.1103/PhysRevD.100.041901>.
- [15] S. Goldstein, J. L. Lebowitz, R. Tumulka, and N. Zanghì, “Canonical typicality,” *Physical Review Letters* **96** no. 5, (Feb, 2006) . <http://dx.doi.org/10.1103/PhysRevLett.96.050403>.
- [16] D. N. Page, “Average entropy of a subsystem,” *Physical Review Letters* **71** no. 9, (Aug, 1993) 1291–1294. <http://dx.doi.org/10.1103/PhysRevLett.71.1291>.
- [17] G. Raggioa, “Properties of q-entropies,” *J. Math. Phys* **36** no. 9, (1995) .
- [18] K. M. R. Audenaert, “A sharp continuity estimate for the von neumann entropy,” *Journal of Physics A: Mathematical and Theoretical* **40** no. 28, (Jun, 2007) 8127–8136.
<https://doi.org/10.1088/1751-8113/40/28/s18>.
- [19] X. Chen and A. W. W. Ludwig, “Universal spectral correlations in the chaotic wave function and the development of quantum chaos,” *Physical Review B* **98** no. 6, (Aug, 2018) .
<http://dx.doi.org/10.1103/PhysRevB.98.064309>.
- [20] P. Calabrese and J. Cardy, “Evolution of entanglement entropy in one-dimensional systems,” *Journal of Statistical Mechanics: Theory and Experiment* **2005** no. 04, (Apr, 2005) P04010.
<http://dx.doi.org/10.1088/1742-5468/2005/04/P04010>.
- [21] H. Liu and S. J. Suh, “Entanglement tsunamis: Universal scaling in holographic thermalization,” *Physical Review Letters* **112** no. 1, (Jan, 2014) .
<http://dx.doi.org/10.1103/PhysRevLett.112.011601>.
- [22] M. Fagotti and F. H. L. Essler, “Reduced density matrix after a quantum quench,” *Physical Review B* **87** no. 24, (Jun, 2013) . <http://dx.doi.org/10.1103/PhysRevB.87.245107>.
- [23] T. Koffel, M. Lewenstein, and L. Tagliacozzo, “Entanglement entropy for the long-range ising chain in a transverse field,” *Phys. Rev. Lett.* **109** (Dec, 2012) 267203.
<https://link.aps.org/doi/10.1103/PhysRevLett.109.267203>.
- [24] F. Verstraete and J. I. Cirac, “Matrix product states represent ground states faithfully,” *Phys. Rev. B* **73** (Mar, 2006) 094423. <https://link.aps.org/doi/10.1103/PhysRevB.73.094423>.
- [25] K. Mitarai, M. Negoro, M. Kitagawa, and K. Fujii, “Quantum circuit learning,” *Physical Review A* **98** no. 3, (Sep, 2018) . <http://dx.doi.org/10.1103/PhysRevA.98.032309>.
- [26] J.-G. Liu, Y.-H. Zhang, Y. Wan, and L. Wang, “Variational quantum eigensolver with fewer qubits,” *Phys. Rev. Research* **1** (Sep, 2019) 023025.
<https://link.aps.org/doi/10.1103/PhysRevResearch.1.023025>.

- [27] B. T. Gard, L. Zhu, G. S. Barron, N. J. Mayhall, S. E. Economou, and E. Barnes, “Efficient symmetry-preserving state preparation circuits for the variational quantum eigensolver algorithm,” *npj Quantum Information* **6** no. 1, (Jan, 2020) . <http://dx.doi.org/10.1038/s41534-019-0240-1>.
- [28] S. Sim, P. D. Johnson, and A. Aspuru-Guzik, “Expressibility and entangling capability of parameterized quantum circuits for hybrid quantum-classical algorithms,” *Advanced Quantum Technologies* **2** no. 12, (Oct, 2019) 1900070. <http://dx.doi.org/10.1002/qute.201900070>.
- [29] D. Gross, S. T. Flammia, and J. Eisert, “Most Quantum States Are Too Entangled To Be Useful As Computational Resources,” *Physical Review Letters* **102** no. 19, (May, 2009) . <http://dx.doi.org/10.1103/PhysRevLett.102.190501>.
- [30] A. W. Harrow, L. Kong, Z.-W. Liu, S. Mehraban, and P. W. Shor, “A Separation of Out-of-time-ordered Correlation and Entanglement,” [arXiv:1906.02219](https://arxiv.org/abs/1906.02219) [quant-ph].
- [31] T. Rakovszky, F. Pollmann, and C. von Keyserlingk, “Sub-ballistic Growth of Rényi Entropies due to Diffusion,” *Physical Review Letters* **122** no. 25, (Jun, 2019) . <http://dx.doi.org/10.1103/PhysRevLett.122.250602>.
- [32] M. Žnidarič, “Entanglement growth in diffusive systems,” *Communications Physics* **3** no. 1, (Jun, 2020) . <http://dx.doi.org/10.1038/s42005-020-0366-7>.
- [33] M. Mezei and D. Stanford, “On entanglement spreading in chaotic systems,” *Journal of High Energy Physics* **2017** no. 5, (May, 2017) . [http://dx.doi.org/10.1007/JHEP05\(2017\)065](http://dx.doi.org/10.1007/JHEP05(2017)065).
- [34] M. Broughton, G. Verdon, T. McCourt, A. J. Martinez, J. H. Yoo, S. V. Isakov, P. Massey, M. Y. Niu, R. Halavati, E. Peters, M. Leib, A. Skolik, M. Streif, D. V. Dollen, J. R. McClean, S. Boixo, D. Bacon, A. K. Ho, H. Neven, and M. Mohseni, “TensorFlow Quantum: A Software Framework for Quantum Machine Learning,” [arXiv:2003.02989](https://arxiv.org/abs/2003.02989) [quant-ph].
- [35] L. Biewald, “Experiment Tracking with Weights and Biases,” 2020. <https://www.wandb.com/>. Software available from wandb.com.